LUND UNIVERSITY
Faculty of Science

Extending the spectral range of THz quantum cascade lasers

Yutian Song

Thesis submitted for the degree of Master of Science
Project duration: 8 months

Supervised by Andreas Wacker

Department of Physics
Division of Mathematical Physics
May 2024

Abstract

Recently, substantial progress has been made on the temperature performance of Terahertz Quantum Cascade Lasers (THz QCLs) around frequencies of 4 THz. The project shall study whether similar results can be obtained in a wider spectral range. For this purpose, detailed simulations were performed based on the nonequilibrium Green's function model developed earlier in the group. The main issue is to identify which features limit the performance of THz QCLs. This thesis work is theoretical, the results of the studies are compared to experimental measurements when this is possible*.

*The content, findings and text of the thesis are results of my work. Syntax and grammar of the text have been polished with the aid of Chatgpt.

Acknowledgements

First and foremost, I really want to thank my supervisor Andreas Wacker for taking great amount of his time to supervise and teach me about the fascinating area of THz Quantum Cascade Lasers. Secondly, I would like to thank Ali Razavipour and Seyed Ghasem for always being available for discussion and making the project even more enjoyable. Also, I would like to thank Claudio Verdozzi for taking his time to examine the project. Last but not least, many thanks to the Mathematical Physics department for the welcoming atmosphere and the free coffee.

List of Acronyms

THz: Terahertz

QCL: Quantum Cascade Laser

MBE: Molecular-Beam Epitaxy

ULS: Upper Laser state

LLS: Lower Laser State

RT: Resonant Tunneling

LO-Phonon: Longitudinal Optical-Phonon

NEGF: Non- Equilibrium Green's Function

CBO: Conduction Band Offset

ac: alternating current

dc: direct current

Content

1 Introduction

The range of electromagnetic waves spanning from 0.1 THz to 10 THz (wavelengths from 30μm to 3000μm) is commonly denoted as terahertz waves, representing the transitional domain between infrared and microwave frequencies. Terahertz waves boast attributes such as formidable penetrability, and low photon energy. As a result, they find diverse applications across radar communications, security screenings, biomedicine, environmental monitoring, and military operations [1]. However, despite its technological potential, this spectral band is often dubbed the 'THz gap' due to the challenges in efficient generation, modulation, and detection of THz waves [2]. Hence, the development of THz quantum cascade lasers (QCLs) is pivotal, given their compactness, low energy consumption, facile integration, and tunability compared to alternative terahertz sources, e.g. photonic sources. Progress in this area holds significant promise across various domains, including biomedical imaging [3][4], terahertz communication technology [5], security measures [5], and counter-terrorism efforts [5]. Consequently, enhancing the performance of THz QCLs stands as a paramount objective for the future. The efficacy of THz QCLs hinges greatly upon operating temperature, frequency tuning range, and output power [6].

In 2002, R. Köhler et al. developed the world's first THz quantum cascade laser (QCL), operating at a luminous frequency of 4.4 THz [7]. Since then, THz QCL techniques have advanced significantly, with operating frequencies now spanning from 0.8 to 5.6 THz [8][9]. In 2020, Ali Khalatpour et al. achieved a breakthrough with a portable THz QCL boasting a maximum operating temperature of 250 K, operating at 4 THz, and featuring a two-well design [10]. At the heart of the THz QCL design lies its active region, where GaAs/$Al_xGa_{1-x}As$ material systems are used for the majority of THz QCL active regions, employing various structural designs. GaAs/$Al_xGa_{1-x}As$ represents a highly developed III-V group material system, characterized by near-perfect lattice matching and minimal strain, facilitating the growth of high-quality epitaxial structures. By adjusting the Al and Ga components in GaAs/$Al_xGa_{1-x}As$, suitable intersubband energy levels and wavefunctions in the conduction band can be selected for intersubband transitions within the THz band. Through the implementation of Molecular-Beam Epitaxy (MBE) techniques, alternating growth of $Al_xGa_{1-x}As$ and GaAs layers with precise periodicity enables the creation of quantum wells. This periodicity results in the formation of multiple repetitive modules, where electrons are injected from the preceding module, emitting photons of specific frequencies through stimulated emission, and subsequently injected into the succeeding module. This process is constantly cycling (Fig. 1), which can achieve the multiplication of electron injection.

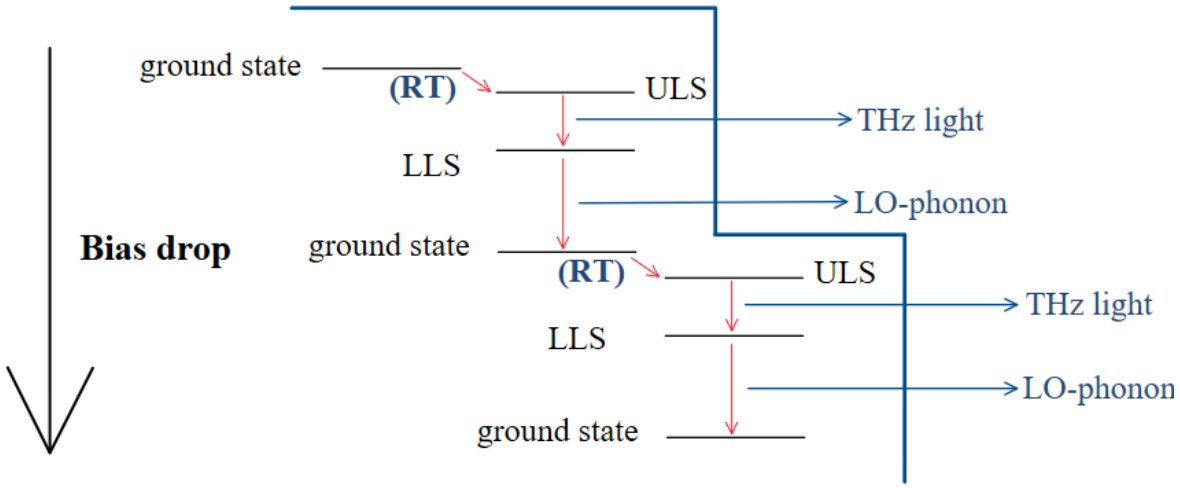

Figure 1: A diagram giving an overview of THz QCL operating principle.

In my project, the primary objective is to identify the factors limiting the performance of THz quantum cascade lasers (THz QCLs) to enhance their efficacy. Additionally, we aim to draw preliminary conclusions regarding the feasibility of THz QCLs operating below 4 THz. To achieve this, comprehensive simulations will be conducted using the nonequilibrium Green's function (NEGF) model previously developed within our research group.

This thesis will start with an introduction to THz QCLs in Chapter 1, providing context for the subsequent discussions. Chapter 2 will delve into the operational principles of THz QCLs, focusing on the active region, scattering phenomena, and waveguide properties. In Chapter 3, we will explore the modification of energy differentials to enhance THz light generation, employing simulations with 3 and 5 energy levels. Chapter 4 will analyze the distribution of current density and electron density, investigating their relationship with gain and the underlying theoretical framework. We will pinpoint the factors directly influencing peak gain and conduct a comparative analysis between experimental and simulated outcomes using the NEGF package. Chapter 5 will investigate the impact of conduction band offset (CBO) modifications on parameters such as highest current density, light frequency, and gain, aiming to elucidate the underlying mechanisms. Finally, Chapter 6 will explore the correlation between sheet doping density and both the highest current density and gain.

2 The operation principle in THz QCL

2.1 An Introduction to THz QCL

The THz quantum cascade laser stands as one of the most efficient electrically pumped semiconductor radiation sources for generating THz waves [11]. Its structure is primarily based on a waveguide, exemplified in Figure 2.

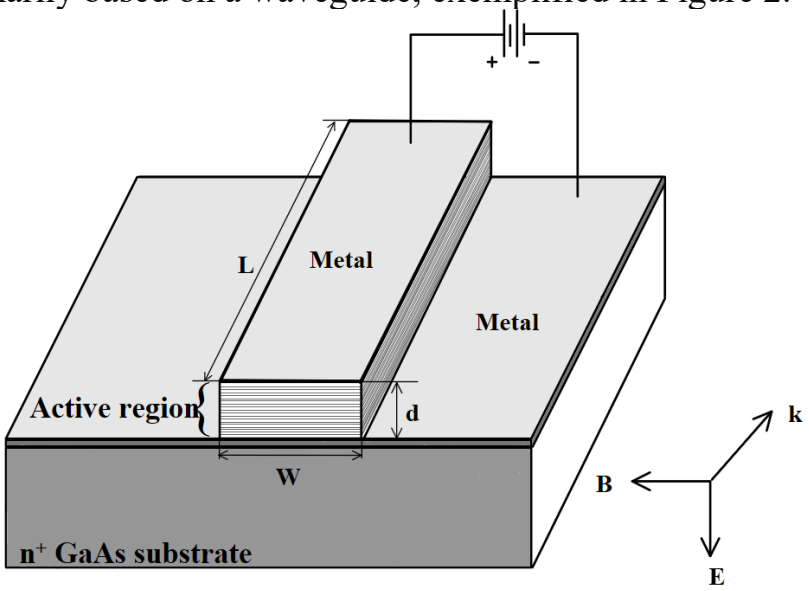

Figure 2: Metal-Metal Waveguide for THz QCL. The top and bottom layers comprise metals connected to the positive and negative terminals of the power supply, respectively. The active region, consisting of multiple layers situated between the metals, is highlighted in the illustration. The bottom of the waveguide is n^+ GaAs substrate. The length L, the thickness d, and the width W of the waveguide are labeled in the figure. The direction of light propagation **k**, the direction of the electric field **E,** and the direction of the magnetic field **B** are all shown in the figure. The growth direction is the opposite direction of **E.**

Metal-metal waveguides offer excellent optical confinement, markedly improving limiting factors compared to semi-insulating surface plasmon waveguides, along with superior thermal conductivity. These advantages become increasingly pronounced with longer wavelengths, rendering metal-metal waveguides highly suitable for generating terahertz light [5]. Like conventional lasers, THz QCLs possess active regions responsible for light amplification, which constitute the core of their operational principles. However, unlike traditional lasers, the active region design of THz QCLs is based on coupled multiple quantum wells.

The active region of THz QCLs typically comprises GaAs/$Al_xGa_{1-x}As$ material systems grown using Molecular-Beam Epitaxy (MBE) techniques. The GaAs/$Al_xGa_{1-x}As$ material constitutes a typical heterogeneous structure, forming a type I heterogeneous junction. Consequently, a one-cycle quantum well is obtained, as depicted in Figure 3.

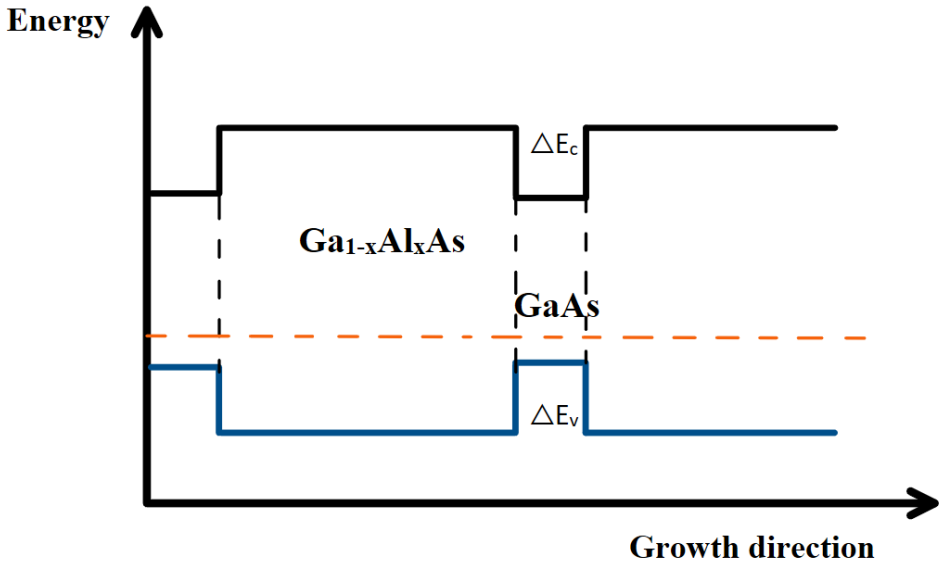

Figure 3: This figure illustrates the conduction band edge energy (black line) and valence band edge energy (blue line) of GaAs/$Al_xGa_{1-x}As$ material along the growth direction, alongside the Fermi energy level (orange dashed line) of the material. The conduction band offset (CBO) and valence band offset (VBO) are indicated.

By alternately growing layers of $Al_xGa_{1-x}As$ and GaAs with consistent periodicity, a series of quantum wells, referred to as a superlattice, can be obtained. In other words, the superlattice consists of multiple layers of thin-film materials arranged in repetitive cycles. A closer examination of a quantum well is provided in Figure 4.

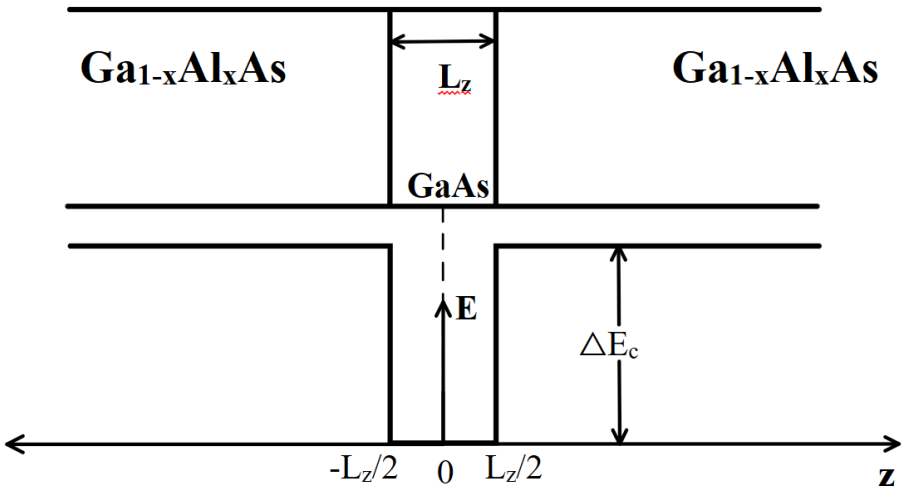

Figure 4: This figure depicts a model comprising three layers of GaAs/$Al_xGa_{1-x}As$ material, with GaAs positioned between two layers of AlxGa1-xAs, along with the corresponding distribution diagram of the conduction band edge energy along the growth direction (i.e., the z-direction). L_z represents the length of one GaAs layer, which also corresponds to the length of the quantum well, while $\triangle E_c$ denotes the conduction band offset resulting from the difference in conduction band edge energy between the two types of layers.

We consider that electron movement primarily occurs within the quantum wells along the growth direction (i.e., the z-direction). When the quantum well is sufficiently high, or 'infinitely high,' the corresponding wavefunction $\varphi(z)$ of electrons satisfies the stationary Schrödinger equation:

$$-\frac{\hbar^2}{2\mathrm{m_n}}\frac{\partial^2}{\partial \mathrm{z}^2}\varphi(\mathrm{z}) + \mathrm{V(z)}\varphi(\mathrm{z}) = \mathrm{E_c}\varphi(\mathrm{z}), \quad (1)$$

Where E represents the energy of the electron and m_n denotes the effective mass of an electron, the potential energy function V(z) governing the movement of electrons can be expressed as follows,

$$\mathrm{V(z)} = \begin{cases} 0 & \left(-\frac{\mathrm{L_z}}{2} < \mathrm{z} < \frac{\mathrm{L_z}}{2}\right) \\ \infty & \left(\mathrm{z} < -\frac{\mathrm{L_z}}{2}, \mathrm{z} > \frac{\mathrm{L_z}}{2}\right) \end{cases}, \quad (2)$$

given a quantum well length of L_z. Since the potential barrier is infinitely high, electrons are confined within the potential well, implying that the wavefunction at $z=\pm L_z/2$ is zero. Exploiting this confinement, the energy of an electron moving in the z direction can only assume discrete values, as shown by:

$$E_n = \frac{(\pi\hbar)^2}{2m_n}\left(\frac{n}{L_z}\right)^2 \qquad n = 1,2,3,\ldots \quad (3)$$

And the corresponding wavefunction is

$$\varphi(z)_n = \sqrt{\frac{2}{L_z}}\, cos\frac{n\pi}{L_z}z \qquad n = 1,2,3,\ldots \quad (4)$$

We got the corresponding different intersubbands for the conduction band which are shown in figure 5 (a). Similarly, this also applies to the valence band. Then, electrons transfer from the conduction intersubband to the valence intersubband or transfer within the conduction interband which we call them interband transition and intersubband transition respectively (Fig. 5(b)). While the THz QCLs, only use intersubband transition, because using intersubband transition doesn't need to consider the band gap energy but not the interband transition leading to intersubband transition requiring only a small amount of energy or frequency when which makes THz frequency possible [12].

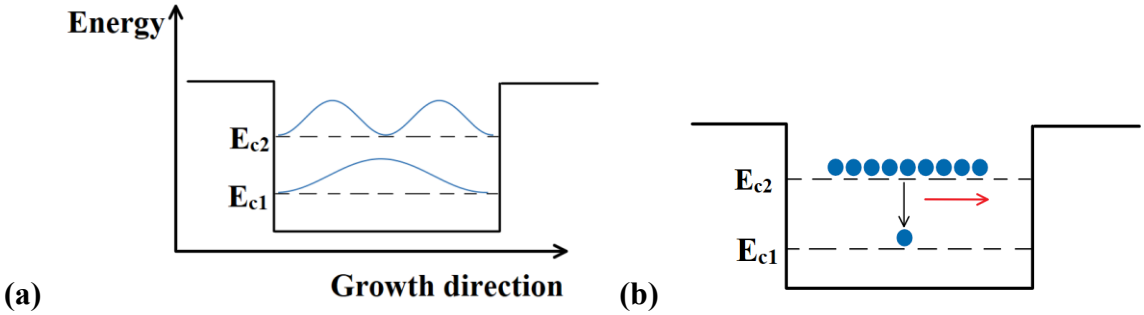

Figure 5: Illustration of intersubbands within the conduction band, showcasing the wavefunction of electrons. (b) Depiction of electron transition pathways in THz QCLs. The red curve illustrates the generation of light.

Electron transitions inherently involve energy transitions which means, for example, we have light coming out due to energy conservation principles, a fact effectively leveraged by THz QCLs. This process is fundamental to the operation of the active region within THz QCLs, constituting its core functionality.

2.2 Active region

The active region of THz QCLs is meticulously engineered to achieve population inversion, accomplished by fine-tuning the energy levels of multiple quantum wells, scattering rates, and wavefunctions to achieve gain at desired frequencies. Population inversion is a prerequisite for laser production, a concept well-established in quantum mechanics. In quantum mechanics, it is known that a periodic perturbation potential can expressed as

$$\hat{V}(t) = \hat{F}e^{-i\omega t} + \hat{F}^{+}e^{i\omega t}, \tag{5}$$

where $\hat{F}$ and $\hat{F}^{+}$ are operators, and ω is frequency of the perturbation. The transition probability from an initial state (a) to the final state (b) is

$$\Gamma_{a\to b} = \frac{2\pi}{\hbar}\left|\langle b^0|\hat{F}|a^0\rangle\right|^2\delta(E_b^0 - E_a^0 - \hbar\omega) + \frac{2\pi}{\hbar}\left|\langle b^0|\hat{F}^{+}|a^0\rangle\right|^2\delta(E_b^0 - E_a^0 + \hbar\omega), \tag{6}$$

Only when $E_b^0 = E_a^0 + \hbar\omega$ or $E_b^0 = E_a^0 - \hbar\omega$, which corresponds to the absorption or emission of the energy quantum $\hbar\omega$ from or to the oscillating field [13], respectively, the transition probability is non-zero. As shown in Ref. [14] the transition probability from the initial to the final state is proportional to $\frac{1}{\tau_a}$, where τ_a represents the lifetime of electrons in the initial state.

Various designs of the active region structure exist, differing primarily in the number of quantum wells and energy levels. The simplest structure entails two quantum wells and three energy levels which are shown in Fig. 6, corresponding to the upper laser state (ULS) (red curve), lower laser state (LLS) (blue curve), and ground state (green curve) within a module. Consequently, in this scenario, the initial state can be LLS, and the final state, the ground state.

Now we focus on the transitions between the LLS and the ground state, where the energy mismatch is typically by the emission of optical phonons, providing the oscillating potential in Eq. (5). So, we know that the first term of Eq. (6) is proportional to n_{ph}, representing the rate of phonon occupation indicative of absorption. Conversely, the second term of Eq. (6) is proportional to $n_{ph}+1$, representing spontaneous emission and simulation emission. These relationships guide our understanding and analysis.

$$-\dot{n}_L = \frac{1}{\tau_L}\left[\left(n_{ph}+1\right)n_L - n_{ph}n_g\right], \tag{7}$$

Where $\dot{n}_L$ is the density of electrons in LLS, τ_L is the lifetime of the electrons in LLS, n_L and n_g are number of electrons on LLS and ground state respectively. In equilibrium at absolute temperature, we have

$$\left(n_{ph}+1\right)n_L = n_{ph}n_g, \tag{8}$$

So, we get

$$\frac{n_L}{n_g} = \frac{n_{ph}}{n_{ph}+1} = \frac{1}{1+e^{\beta\hbar\omega-1}} = e^{-\beta\hbar\omega} = e^{-\beta(E_L-E_g)} = \frac{e^{-\beta E_L}}{e^{-\beta E_g}}, \tag{9}$$

where $\beta = \frac{1}{kT}$, k is the Boltzmann constant, and E_L and E_g are the energy of LLS and ground state, respectively. Normally, $n_L < n_g$ because $E_L > E_g$ based on Eq. (9) or Boltzmann distribution. And it's the same with ULS and LLS, as $n_U < n_L$ because $E_U > E_L$, no laser is obtained in this case. Laser is the acronym for light Amplification by Stimulated Emission of Radiation. It is laser action that amplifies light through stimulated emission. Therefore, in order to obtain lasing, n_L should be greater than n_g, allowing a sufficient number of electrons on ULS transport to the LLS simulated by oscillating potential provided by ac field or emission of optical phonon. When more electrons occupy the ULS instead of the LLS $n_U - n_L > 0$ we call population inversion.

Figure 6 illustrates three adjacent modules of the active region with 2 wells and 3 energy states, utilizing EZ states for the enhanced definition of ground and upper states, as noted in Ref. [15]. EZ states refer to localized states achieved through basis transformation from the energy eigenstates of each multiplet [15]. Electron transition in this structure follows the principle of resonant tunneling (RT) injection, which outperforms scattering-assisted (SA) injection in designs exceeding 2 THz in the terahertz frequency range [17]. Electrons are injected from

the ground state in the (n-1)th module to the ULS in the nth module within the injection region. Subsequently, electrons transition from the ULS to the LLS while generating THz light [16]. Finally, electrons rapidly move from the LLS to the ground state through longitudinal optical (LO)-phonon emission, known as the direct-phonon method. This process (see Fig.1) facilitates population inversion, as there are more electrons in the ULS than the LLS, representing the most common and efficient method for depopulating electrons in the LLS [17][18]. The production of THz light and LO-phonons is determined by the difference in energy levels, with their frequencies derived from the Planck relation E=$\hbar\omega$, where $\hbar$ is reduced Planck's constant and ω represents the angular frequency of photon or phonon which we can directly get from $\omega = 2\pi\nu$, where ν is frequency of photon or phonon. Hence, the energy difference between energy levels plays a crucial role in determining THz QCL performance.
Moreover, it is worth noting that the reason THz QCL emit optical phonon rather than acoustic phonons is that the energy of optical phonons is more aligned with the energy difference between LLS and the ground state for the GaAs/$Al_xGa_{1-x}As$ material systems which normally is in the tens of meV, while the energy of acoustic phonons is typically below 10 meV.

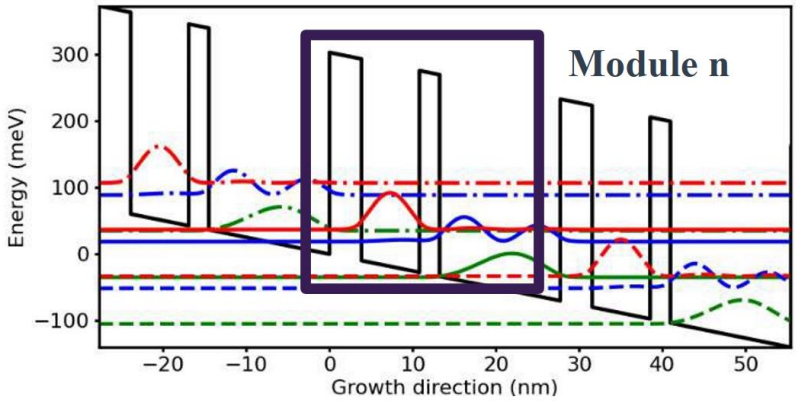

Figure 6: EZ states illustrate the active region structure with 2 wells and 3 energy states. The upper laser state (ULS) is represented by the red line, the lower laser state (LLS) by the blue line, and the ground state by the green line for the nth module. The combination of dotted and dashed lines represents the (n-1)th module, while the (n+1)th module is depicted by a pure dashed line.

Additionally, taking into account more levels of active region structure involves selecting 2 quantum wells and 5 energy levels (See Fig. 7). Electron transition in this case follows a similar pattern to the structure with 3 energy levels, with the addition of two more energy levels, the 4th and the 5th, impacting THz QCL performance. Electrons tunneling to the ULS in the nth module from the ground state in the (n-1)th module, followed by transport from the ULS to the LLS while generating THz light. Subsequently, electrons rapidly move from the LLS to the

ground state via LO-phonon emission, similar to the process described for the simpler structure. However, electrons in the ULS may scatter or absorb LO-phonons to the 5th or 4th energy level, and electrons in the LLS may also scatter or absorb LO-phonons to the 4th level. Notably, electrons in the ULS for the nth module may tunnel to the 4th energy level for the (n+1)th module, which is undesirable as it reduces the efficiency of THz light generation. Thus, designing the active region structure to ensure that the 4th and 5th energy levels are sufficiently high to minimize electron transport to these levels from the ULS and LLS is crucial, a topic that will be further explored in the subsequent section.

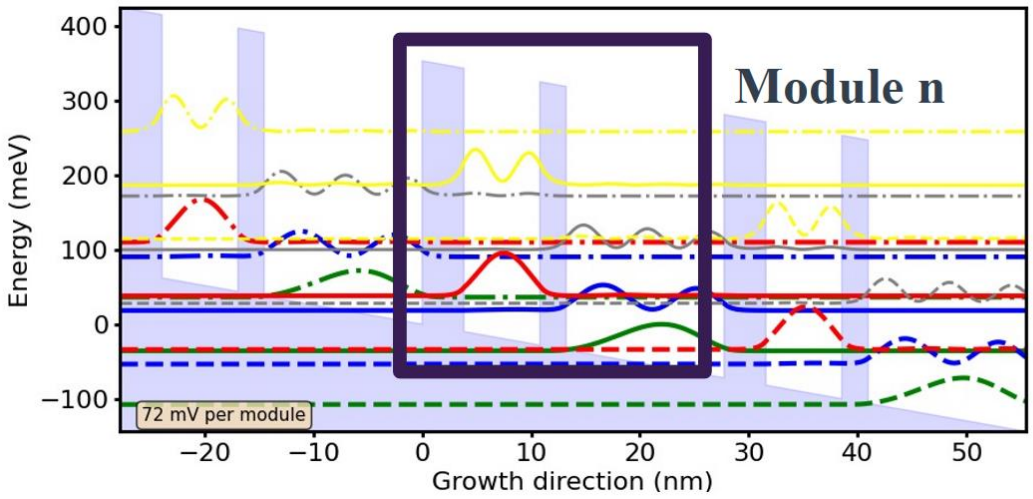

Figure 7: EZ states depict the active region structure with 2 wells and 5 energy states. The ULS is represented by the red line, the LLS by the blue line, the ground state by the green line, the 4th energy level by the grey line, and the 5th energy level by the yellow line for the nth module. The combination of dotted and dashed lines represents the (n-1)th module, while the (n+1)th module is depicted by a pure dashed line.

2.3 Scattering

Various types of scattering can impede the smooth transfer of electrons from the upper laser state (ULS) to the lower laser state (LLS), such as electron-electron scattering [16] and average electron scattering rate including various electron-related scattering events such as electron-phonon scattering, electron-impurity scattering and etc. These scattering events are detrimental to efficient terahertz (THz) light generation and result in reduced gain. Thus, minimizing these scatterings is crucial for enhancing THz light generation efficiency.

Several factors influence these scattering phenomena. For instance, the research highlighted in Ref. [27] demonstrates that electron-electron scattering rates and average scattering rates are influenced by multiple factors. Firstly, both the electron-electron scattering rate and average scattering rate increase with the widening of the quantum well. This increase is attributed to the decreasing

energies of electrons both in the ULS and LLS within the well as its width increases. Consequently, the energy level difference diminishes, leading to a decrease in transfer energy during scattering and subsequently increasing the scattering rate and average scattering rate.

Secondly, while the average scattering rate of electron-electron interactions shows a slight decrease with increasing electron temperature, the effect is not pronounced. This suggests that electron temperature has a limited impact on the average scattering rate within the well. However, the increase in electron temperature elevates the kinetic energy of electrons, consequently increasing the transfer energy during scattering events, resulting in a slight decrease in the average scattering rate. Moreover, the average scattering rate of electron-electron interactions increases with the rise in charge carrier concentration, as higher carrier concentrations foster closer interactions between electrons, thereby facilitating more frequent energy transfers during scattering events.

Additionally, the scattering rate of electron-electron interactions within the well decreases with the strengthening of an applied dc electric field. This reduction occurs because scattering between electrons from ULS to LLS constitutes symmetric scattering, which refers to a phenomenon in which the scattering process exhibits inherent symmetries of the system or the scattering potential. So, it is attenuated by the presence of an external electric field, resulting in a decrease in the electron-electron scattering rate with increasing field strength.

Furthermore, Ref. [17] emphasizes that Interface Roughness (IFR) scattering arises from imperfect or rough interfaces formed during material growth. This phenomenon induces non-radiative transitions from ULS to LLS, thereby reducing gain and increasing current.

2.4 Waveguide

A waveguide is a structure that guides electromagnetic waves from one point to another, typically with minimal loss of energy by confining the wave within specific boundaries. A well-designed waveguide structure is essential for optimal optical confinement, reducing the threshold current density of the laser and enhancing slope efficiency [20]. Essentially, it minimizes losses during optical transmission. The threshold condition for laser excitation occurs when the gain equals the total losses, expressed by the equation:

$$g_{th}\Gamma = \alpha_m + \alpha_\omega, \quad (10)$$

Here, g_{th} represents threshold gain, Γ denotes the optical confinement factor, α_m signifies mirror losses, and α_ω represents waveguide losses—these being the four fundamental parameters of a laser [21]. A metal-metal waveguide shown in Fig. 2, with an overlap factor close to unity ($\Gamma \approx 1$) and low waveguide losses

(α_ω), effectively confines THz light [5].

The dimensions of the waveguide significantly impact the propagation of terahertz light. The relationship:

$$\Delta f = \frac{\Delta\omega}{2\pi} = \frac{c}{2nL}, \tag{11}$$

where Δf is change in frequency of light, $\Delta\omega$ is change in angular frequency of light, c is light speed, n is refractive index of material and L is length of waveguide which is described in the Fig. 2. Because of the existence of lifetime of electrons, electrons more likely occupy the lower energy state, resulting in a smaller frequency of THz light generated from the active region at the same time. According to the Eq. (11), we can see that the length of the waveguide can help us to distinguish between different frequencies of THz light in the waveguide, the longer the waveguide, the harder it's for us to distinguish between these frequencies [22] because the change in frequency of light is too small. But if the waveguide is shorter, the more losses we might have due to mirror losses. The thickness of the waveguide determines the number of layers of material. If d is too large, the module wave functions would leak out. But, if d is too short, the boundary condition would affect the states in the module [23]. The width of the waveguide determines the current of the metal. Therefore, the size of the waveguide is really important.

2.5 Doping

In nature, perfect crystals are rare, and semiconductor crystals are no exception—they invariably contain defects. These defects disrupt the periodic potential field created by the precisely arranged crystal atoms, thereby introducing new electronic energy levels in semiconductors. This disruption can significantly influence the electrical conductivity and other characteristics of semiconductors. In contrast to defects, impurity atoms can be precisely controlled. The type, concentration, distribution, and other characteristics of impurities can be manipulated using appropriate methods during the semiconductor crystal preparation process, enabling more precise control over the semiconductor's electrical conductivity. Hence, in practical engineering, doping is often employed to achieve desired semiconductor properties. Doping is the deliberate introduction of impurities into a semiconductor to regulate its properties. Impurities are typically introduced through substitutional doping, where impurity atoms replace original lattice site atoms. Although the introduced impurity atoms often possess different atomic structures from the original semiconductor atoms, their valence electron structures usually closely resemble each other. In our GaAs/$Al_xGa_{1-x}As$ material, we utilize Si doping in the doping region, as indicated in Fig. 8. During doping, Si atoms replace Ga atoms, resulting in an excess electron and forming an n-type semiconductor. These excess electrons from the doping region tunnel to

the next upper laser state (ULS) module, facilitating the generation of additional terahertz light.

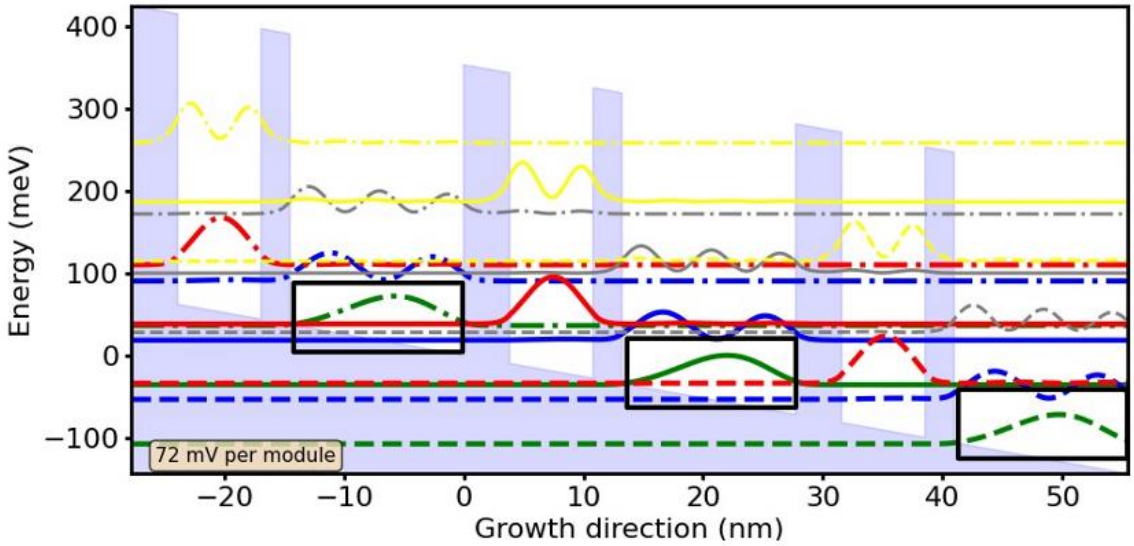

Figure 8: Doping area is marked by black square.

3 Modification of energy difference

The modification of energy differences plays a pivotal role in various experimental outcomes, ranging from determining the frequency of emitted terahertz light in THz QCLs to dictating the emission of photons or phonons and even enhancing the efficiency of terahertz light generation. The emission condition is defined by $\Delta E=h\upsilon$, where ΔE denotes the energy difference and υ represents the frequency of photons or phonons. For context, the frequency of optical phonons in $Al_xGa_{1-x}As$ typically falls around 8 THz. By modifying the energy difference, we can also mitigate the thermal backfilling effect, a significant factor limiting THz QCL performance.

Thermal backfilling involves electrons transitioning back to the lower lasing state (LLS) from the ground state by absorbing a LO-phonon [19], resulting in $\Delta N = n_U - n_L < 0$. This process is influenced by the difference in energy levels. According to Eq. (6), if thermal backfilling occurs, the first term of Eq. (6) becomes larger than the second term, diminishing population inversion. Consequently, thermal backfilling hinders the efficient generation of terahertz photons, as the increased electron population in the LLS reduces the difference in electron population between the upper lasing state (ULS) and LLS, denoted as ΔN. This makes it challenging for electrons from the ULS to efficiently transition to the LLS and ground state levels.

In this chapter, we will explore a structure comprising 3 energy levels with 2 quantum wells, as is described in Ref. [16] to observe changes in energy differences between different states when we vary the value of aluminum fraction in the barriers (x) and bias drop (eFd) to efficiently generate the THz light. Subsequently, we will investigate 5 energy levels with 2 quantum wells, to examine similar energy differences and mitigate thermal backfilling.

3.1 Simulation result for 2-wells and 3 energy levels

We use python 3.8 with EZ state calculation to explore various parameter sets of the THz QCL structure with 2 wells and 3 energy levels, and to access in this way the impact on thermal backfilling (Table. 1).

x	N_{nu}	N_{per}	Number of z-point	eFd (meV)	Thickness of layers (Å)
0.05-0.45	3	3	300	0.072	38.4, 69.7,24.2,**145**

Table 1: Parameter setting for simulation on THz QCL structure with 2-wells and 3 energy levels. x represents Aluminum fraction in the barriers. Bold denotes the thickness of phonon wells (the biggest quantum well in Fig. 7). N_{nu} denote as Number of levels, N_{per} denote as number of modules to extend. eFd we denote as bias drop.

Firstly, we only vary the value of x in GaAs/$Al_xGa_{1-x}As$, leaving other parameters unchanged. We took x from 0.05 to 0.45 at intervals of 0.05. The reason we do not take a number greater than 0.45 is because for x, the electrons in the ground state may not be able to tunnel to the next ULS.

In Fig. 9, we show the relationship between aluminum fraction the barrier (x) and energy difference E_l-E_g, E_u-E_l and $E_{g'}$-E_u-E_l. The reason we plot E_l-E_g is that we would like to find its maximum value so that we could reduce thermal backfilling effect, since then the electrons hardly transport back to LLS from the ground state. And we plot E_u-E_l because we would like to find the minimum value of it so that we could try to find the frequency of light smaller than 4 THz. Moreover, the reason we plot $E_{g'}$-E_u-eFd is that we would like to find its value near 0, so then we can make electrons tunneling to ULS from the last module of the ground state. Fig. 9 shows that as x increases, E_l-E_g rapidly rises initially before stabilizing after reaching 0.3. Meanwhile, E_u-E_l exhibits a decreasing trend, albeit remaining relatively unchanged overall. $E_{g'}$-E_u-eFd initially decreases rapidly, approaching negative values close to zero after 0.3, indicating peak current density is achieved at this point. The proximity of the previous module's ground state energy level to the current module's ULS facilitates efficient electron transport, leading to peak current generation. Figure 6 further confirms the close proximity of each ground state to the ULS of the subsequent module, consistent with our data.

Furthermore, beyond x=0.3, El-Eg remains sufficiently large compared to other x values, making it challenging for electrons to transition from the ground state to the LLS due to thermal backfilling effects. This suggests that values greater than x=0.3 can help reduce thermal backfilling effects.

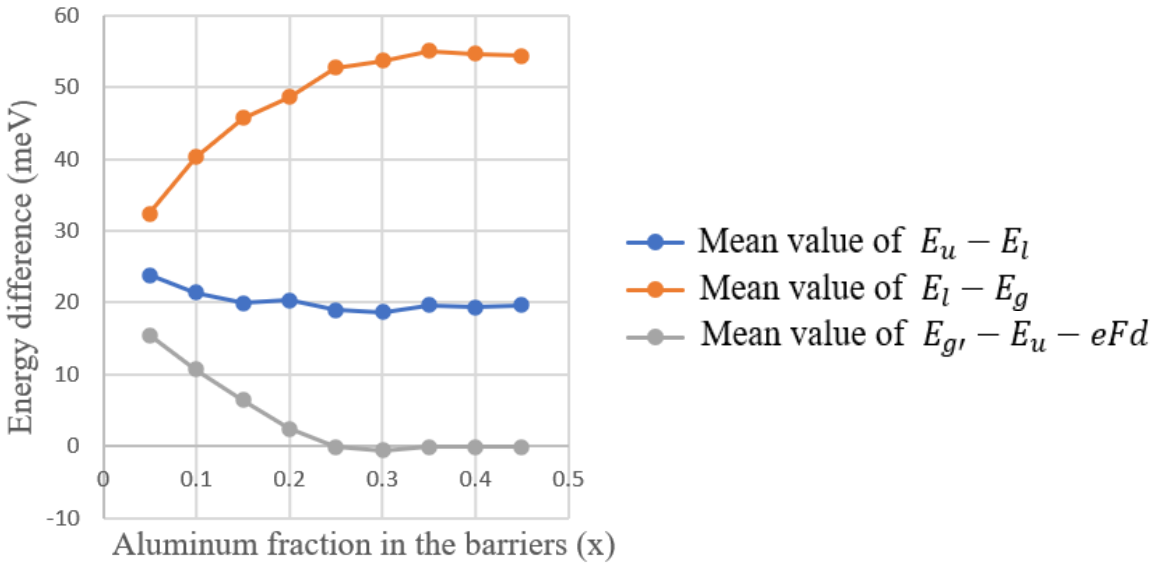

Figure 9: Relationship between Aluminum fraction in the barriers (x) and mean value of energy difference. Blue curve: mean value of energy difference between ULS and LLS under three modules. Orange curve: mean value of energy difference between LLS and ground state under three modules. Grey curve: mean value of energy difference between ground state from last module which noted as g' and ULS under current module, in addition, subtract the value of eFd.

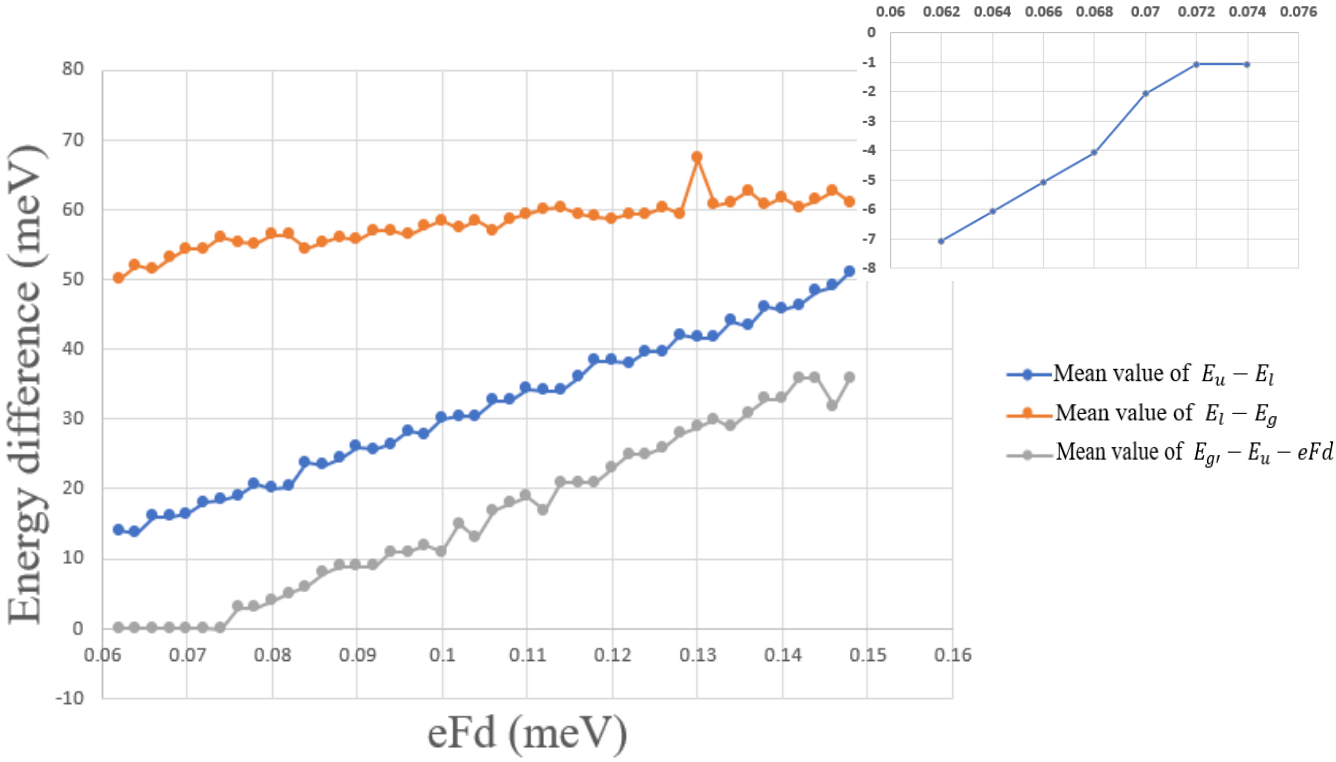

Figure 10: Relationship between bias drop (eFd) and mean value of energy difference. Blue curve: mean value of energy difference between ULS and LLS under three modules. Orange curve: mean value of energy difference between LLS and ground state under three modules. Grey curve: mean value of energy difference between ground state from last module and ULS under current module, in addition, subtract the value of eFd. Insect: relationship between eFd (from 0.062-0.074) and mean value of $E_{g'}$ -E_u-eFd.

In Figure 10, it's evident that as eFd increases, E_u-E_l significantly rises, while there's a less pronounced trend of increase in E_u-E_l. Concurrently, $E_{g'}$ -E_u-eFd gradually increases with the rise in eFd, with the first three simulated data points being negative and close to zero. This indicates the attainment of the highest current density, as discussed previously. Additionally, although E_l-E_g remains relatively stable as eFd increases, smaller eFd values correspond to smaller Eu-El values, potentially aiding in reducing thermal backfilling effects. Hence, an eFd value around 0.074meV is deemed optimal for mitigating thermal backfilling effects, since we could see from the insect that the corresponding $E_{g'}$ -E_u-eFd at 0.074 is the closest one to the zero, which value we need to consider first. And the corresponding E_l-E_g is high enough compared with E_u-E_l.

In conclusion, we observed that both x and bias drop influence energy differences equally, and a combination of x=0.3 and eFd is around 0.074meV appears to yield the highest current density, effectively facilitating THz light generation while reducing thermal backfilling effects in structures with 2-wells and 3 energy levels.

3.2 Simulation result for 2-wells and 5 energy levels

We then consider an active region structure with 2-wells and 5 energy levels which is closer to the real situation, choosing parameters for generating terahertz light more efficiently. We tried different parameters of the structure of THz QCL 2-wells and 5 energy levels to observe which value is the optimal one for generating the THz light.

We only vary the value of x in GaAs/$Al_xGa_{1-x}As$, leaving others parameters unchanged. We took x from 0.15 to 0.45 at intervals of 0.05. And the reason that we do not take a number smaller than 0.15 since for x at this point in time, some values of energy level are above the barrier height (Table. 2).

x	N_{nu}	N_{per}	Number of z-point	eFd (meV)	Thickness of layers (Å)
0.05-0.45	5	3	300	0.072	38.4, 69.7,24.2,**145**

Table 2: Parameter setting for simulation on THz QCL structure with 2-wells and 5 energy levels. x represents Aluminum fraction in the barriers, bold denotes the thickness of phonon wells.

From Fig. 11, we can observe that both E_5-E_u and E_4-E_u increase overall with the increase of x. The sharp increase in the data corresponding to x=0.2 for E_4-E_u, bigger than E_5-E_u is because the 4^{th} level and the 5^{th} level are beyond the conduction band which makes it different from other results of x and make the

point at x=0.2 does not provide useful information for our final results. Therefore, E_4-E_u still increase with the rise of eFd. Meanwhile, E_u-E_l, E_l-E_g and $E_{g'}$ -E_u-eFd show similar trends to the results displayed by our 3 energy levels. E_u-E_l remains relatively constant, while $E_{g'}$ -E_u-eFd raises with add of x, reaching close to zero at x=0.3, indicating the attainment of the highest current density at this point. The consistency of the results between 3 energy levels and 5 energy levels indicates that our conclusion drawn from simulating the 3 energy levels are correct. Since the simulation of 5 energy levels is closer to real data, considering the structural changes starting from the simpler 3-level system is justified in influencing the experimental results.

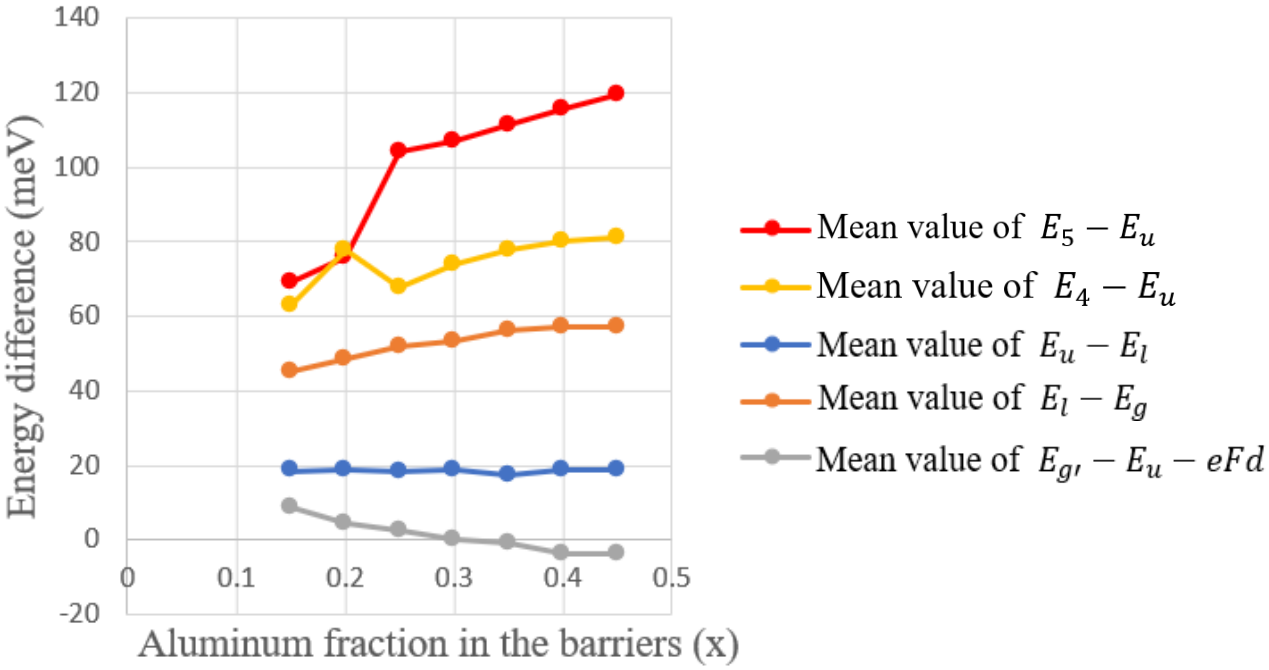

Figure 11: Relationship between Aluminum fraction in the barriers (x) and mean value of energy difference. Red curve: mean value of energy difference between 5th level and ULS under three modules. Yellow curve: mean value of energy difference between 4th level and ULS under three modules. Blue curve: mean value of energy difference between ULS and LLS under three modules. Orange curve: mean value of energy difference between LLS and ground state under three modules. Grey curve: mean value of energy difference between ground state from last module and ULS under current module, in addition, subtract the value of eFd.

For the active region with 2-wells and 5 energy levels, we finally found that x around 0.3 would be the best Aluminum fraction in the barriers for getting the highest current density. And at this point, E_u-E_l is relatively small and E_l-E_g is relatively large, which could help us reduce thermal backfilling effects as well. Additionally, E_5-E_u and E_4-E_u are also rather large, indicating that electrons are less likely to be transported to the 4th and 5th energy level helping us efficiently generate THz light to get good performance of THz QCL.

Overall, in our simulations, we discovered that adjusting the Aluminum fraction in the barriers (x) and the bias drop (eFd) effectively modifies the energy difference, aligning with theoretical discussions outlined in Ref. [28] and Ref. [29]. These adjustments contribute to enhancing the performance of THz QCLs.

The resemblance in behavior between the 5-level and 3-level models suggests that despite the simplified nature of the 3-level model, its simulation outcomes remain insightful and applicable to real-world scenarios.

4 The effect of electron and current density on gain

Gain plays a crucial role in THz QCLs, serving as the primary physical quantity describing the amplification of the light field. Therefore, enhancing gain is the ultimate goal for improving THz QCLs' performance.

Only when we consider non-equilibrium can we have gain. Once we take into account perturbations, our electric field not only consists of the static electric field $\mathrm{E_0}$, but the total electric field becomes time dependent $\mathrm{E(t) = E_0 + E(\omega)e^{-i\omega t}}$, where $\mathrm{E(\omega)e^{-i\omega t}}$ expresses dynamical electric field. Correspondingly, our current density also changes from the static current density $\mathrm{J_0}$ to the total current density $\mathrm{J(t) = J_0 + J(\omega)e^{-i\omega t}}$. We have deduced from the theory that dynamical current density is related to the gain, which Ref. [24] has fully discussed, because gain in the simulation can be expressed as

$$G(\omega) = -\frac{\omega n_r}{c}\Im\{\chi^{rel}(\omega)\}, \tag{12}$$

Where ω is frequency of the light and n_r should be relative refractive index, $\chi^{rel}(\omega)$ is relative susceptibility. And current density can be expressed as

$$J(\omega) = -i\omega P(\omega), \tag{13}$$

Also, polarization density can be expressed as

$$P(\omega) = \epsilon_r \epsilon_0 \chi^{rel}(\omega) E(\omega), \tag{14}$$

Where ϵ_r and ϵ_0 are relative permittivity and permittivity of vacuum [24]. Then we can see that $\chi^{rel}(\omega)$ is proportional to $\mathrm{J(\omega)/[E(\omega)\cdot\omega]}$, so $G(\omega)$ will be proportional to the real part of $\frac{\mathrm{J(\omega)}}{\mathrm{E(\omega)}}$. Thus, dynamical current density is linked to gain. However, we previously discussed in the non-perturbed situation that reaching the highest static current implies that we can drive a large number of electrons from the ground state of the previous module to ULS of the next module, thus efficiently lasing abundant terahertz light. Lasing implies the presence of gain, and the gain has to cover the losses. Therefore, we speculate that static current density can influence the gain as well. So, examining how the static current density and electron density distribution change as gain increases is highly interesting and insightful.

We also know that only when electrons are transported from ULS to the LLS can terahertz light be generated. Additionally, generating more population inversion can produce more terahertz light. Therefore, the distribution of electrons also affects the magnitude of gain.

In this chapter, we utilized the NEGF package which is available in the group of Andreas Wacker, Martin Lindskog and David O. Winge documented in Ref. [30] to simulate the distribution of current density, electron density, and gain. We determine the optimal bias drop, temperature, and frequency of light to achieve the highest gain with 2 wells and 5 energy levels. Furthermore, we conducted comparisons between the static current density distribution and electron density distribution at different temperatures, corresponding to scenarios with the highest and lower gains, respectively. Additionally, we compared experimental results for the static current density and gain with simulation results of current density and gain.

4.1 Current density distribution

We adopted a novel simulation design utilizing NEGF to analyze the distribution of current density at temperatures of 238 K and 400 K for a structure (Table. 3).

x	N_{nu}	N_{per}	eFd (meV)	Doped Density (cm^{-3})	Thickness of layers (Å)
0.3	5	300	0.074	1.5×10^{17}	38.4, 69.7,24.2,**145**

Table 3: Parameter setting for simulation on new THz QCL structure with 2-wells and 5 energy levels. x represents Aluminum fraction in the barriers, bold denotes the thickness of phonon wells.

It is worth notice that the reason why we choose bias drop to be 74mV is that 74mV corresponds to a current density which is maximum in this structure. This also can be found by using the simulation. We chose eighteen values from 66mV to 83mV to input into the simulation, eventually finding their corresponding current densities which are shown below.

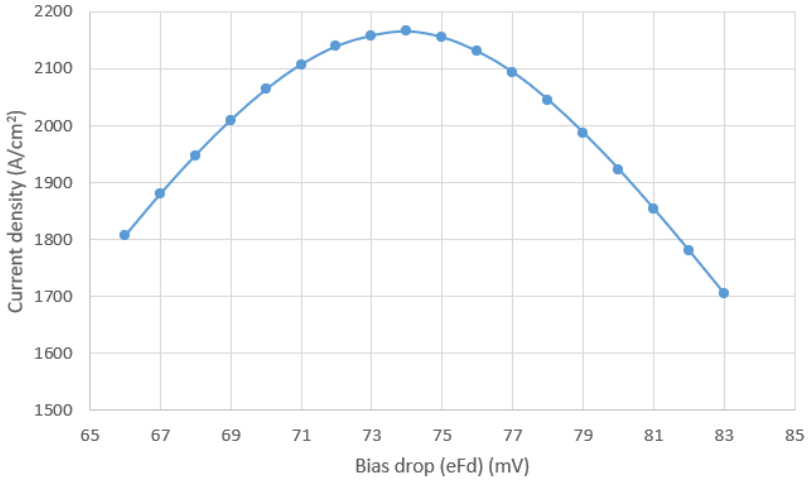

Figure 12: Relationship between bias drop (eFd) and current density (J) at 238K. 74mV corresponds to maximum of current density.

In our simulation, 74mV corresponds to the highest current density. And we have seen that current density is linked to gain due to polarization density. The higher current density, the higher the corresponding gain will be. Why we specifically chose 238 K is that we found that 238 K corresponds to a current density that is at its maximum. To get this, we tried different temperature from 150 K to 400 K simulated in our system by using NEGF, then we got the relationship between current density and temperature is shown down below. We found that 238K is the best temperature since it related to the highest current density then related to the highest gain in this structure.

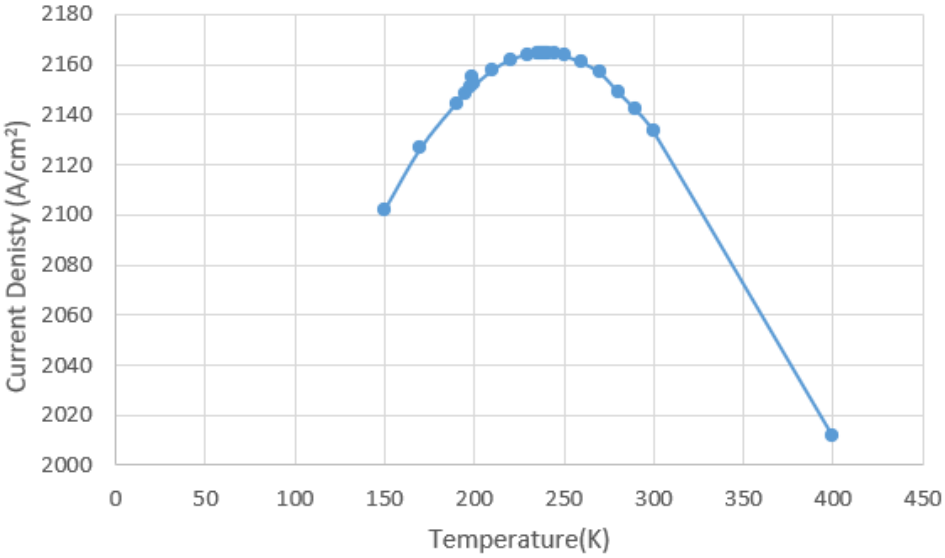

Figure 13: The relationship between current density and temperature. 238 K corresponds to maximum of current density.

The current density distribution at 238 K and 400 K are shown in figure 14 by using NEGF, where we can clearly see that current density at 238 K is higher than the one at 400 K which is consistent with what we said above. And we have also seen in figure 15 that current density mostly above on the injection area and area between ULS and LLS. This is because the electrons need to tunneling to the ULS from the ground state in previous module and tunneling from LLS to ULS, then we have current density. But we still saw some current density above on the upper area which is easy to be observed in the figure 14(b). This is what we called leakage current. We found out that there is more leakage current at 400K than at 238K leading to the smaller current density at 400K than at 238K.

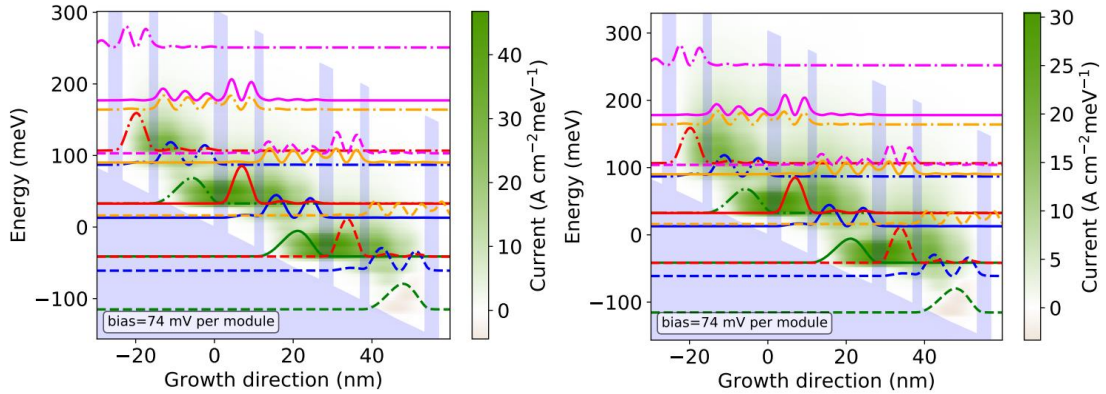

(a) **(b)**

Figure 14: (a) Current density distribution for temperature 238 K. (b) Current density distribution for temperature 400 K.

4.2 Electron density distribution

We can also get electron density distribution at 238 K and 400 K by using NEGF shown in figure 15.

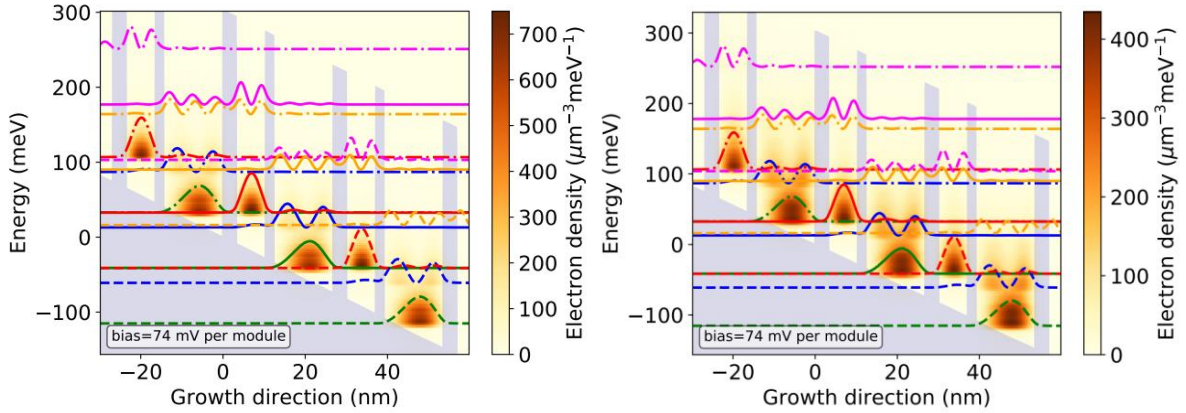

(a) **(b)**

Figure 15: (a) Electron density distribution for temperature 238 K. (b) Electron density distribution for temperature 400 K.

In Fig. 15, we could see that there are more electrons distributed in the states at 238K than 400K which is consist with the previous discussion that there is more current density at 238K than 400K. And we could also observe that electrons drop quickly when we increase energy at 238K comparing to 400K. We can understand why the electron density is distributed like this, by looking at Fermi-Dirac distribution,

$$f(E) = \frac{1}{\exp\left[\frac{E - E_f}{kT}\right] + 1}, \tag{15}$$

where E_f is chemical potential, k is Boltzmann constant and $f(E)$ is the average number of particles in a quantum state of energy E at temperature T. The corresponding function image is shown in Fig. 16. We can see that when the temperature is higher, the curve changes slower. And the energy in a quantum state is bigger than chemical potential, this is because the transitional invariance in (x, y) direction in THz QCL, the wavefunction can be expressed by

$$\psi(\boldsymbol{r}) = \varphi_n(z)\frac{1}{\sqrt{A}}e^{i(k_x x + k_y y)}, \tag{16}$$

While the corresponding energy eigenvalues can be expressed by

$$E = E_n + \frac{\hbar^2 \boldsymbol{k}^2}{2m_n}, \tag{17}$$

where A is the cross-section of the THz QCL and the vector $\boldsymbol{k} = k_x \boldsymbol{e_x} + k_y \boldsymbol{e_y}$ [23]. $\hbar^2 \boldsymbol{k}^2/2m_n$ is kinetic energy which is greater than 0, E_n is the conduction band energy. So, we then know $E - E_n > 0$. Additionally, chemical potential which is also known as fermi energy E_f is smaller than the conduction band energy. Thus $E - E_f > 0$. So, in the figure 16 we only take the part that is $E - E_f > 0$, where we can use it to well explain why at higher temperature the electrons are evenly distributed in the wave shown in figure 15(b).

Such behavior can be well demonstrated by the electron distribution diagrams in the simulation, which indicate that electron density drops with energy quicker at a temperature 238 K than the one at a temperature 400 K. This is consistent with our previous statement that a temperature of 238 K corresponds to the highest current density and therefore the highest gain. Because the faster the electrons density falls off, indicating a greater likelihood of population inversion, and therefore more gain. What's more, we can clearly see that there are some electrons occupying the LLS, which is not what we expected. This happened because of thermal backfilling, as temperature got higher, electrons were more likely to be transported back to LLS from the ground state by absorption of LO-phonon.

Furthermore, we could observe that some electrons are distributed above the LLS, which allows us to explain why we have leakage current at that area.

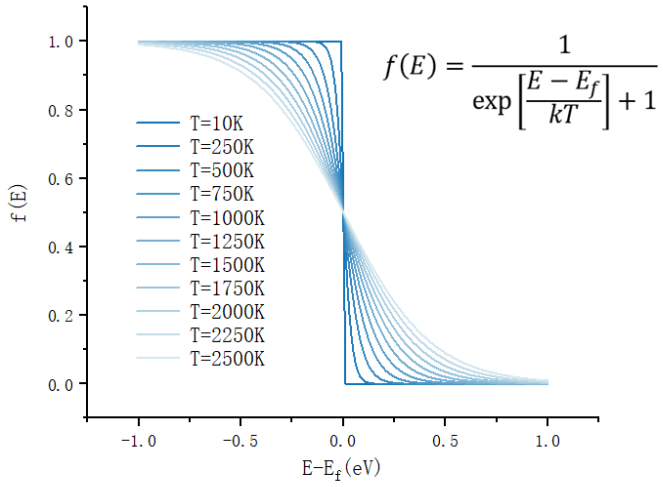

Figure 16: Fermi-Dirac distribution. This figure shows relationship between energy and average number of particles with different temperature from 10 K to 2500 K. Fermi-Dirac distribution function is shown on the graph.

4.3 Peak gain

We have discussed above that 238 K and 74mV correspond to the highest current density in the structure I set, which can be the parameter used for outputting the gain for the structure.

In Fig. 17, we observe that peak gain of intersubband transitions G_p corresponding to 20meV, which we can calculate the frequency of light from $\hbar\upsilon = 20\text{meV}$, which is 4.8 THz. And then we can also know that from Ref. [16] that the peak gain G_p can be expressed by the population inversion between the ULS and LLS ΔN, the oscillator strength f_{ul} and the transition linewidth $\Delta\nu$ as $G_p \propto \Delta N f_{ul}/\Delta\nu$. In fact, the transition linewidth $\Delta\nu$ is defined as $\Delta\nu = \frac{1}{2\pi}\left(\frac{1}{\tau^u} + \frac{1}{\tau^l} + \frac{2}{T^*}\right)$ in which τ^u, τ^l and T^* are the upper-state lifetime, the lower-state lifetime, and pure dephasing times, respectively. $\Delta\nu$ can be related to the full width half maximum (FWHM) as indicated in the Fig.17, as long as we replace the hω to ω in the Fig. 17, then the position of FWHM will be our transition linewidth $\Delta\nu$. Thus, FWHM can be also linked with lifetime of each state. The oscillator strength f_{ul} is wavefunction overlap integral between the ULS and LLS and defined as $f_{ul} = \left(\frac{2m^*\Delta_E}{\hbar^2}\right)|\langle u|z|l\rangle|^2$, in which z is the growth direction, m^* is the effective mass, and Δ_E is the energy separation between the ULS and LLS.

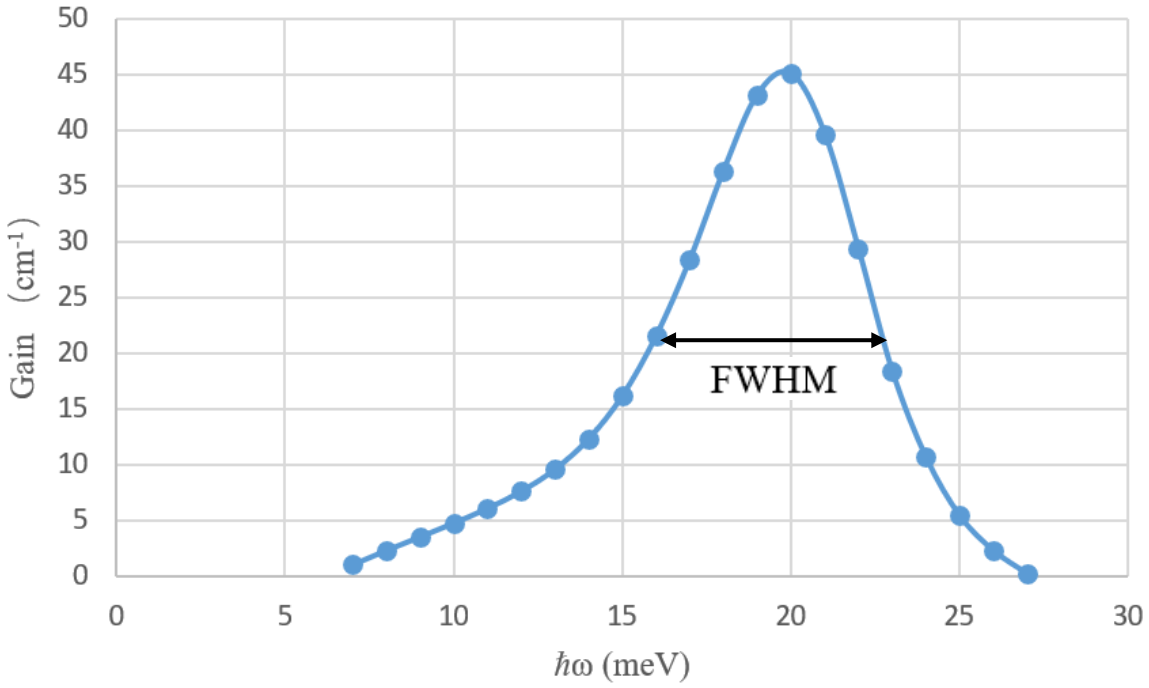

Figure 17: Relationship between $h\omega$ and the gain. 20meV corresponds to maximum of the gain.

4.4 Experiment VS Simulation

After the indications coming from the previous section, we proceed to explore the relationship between phonon temperature and gain across various structures, assessing whether the data we observe are aligned with the experimental findings. Accordingly, we obtained the following graph.

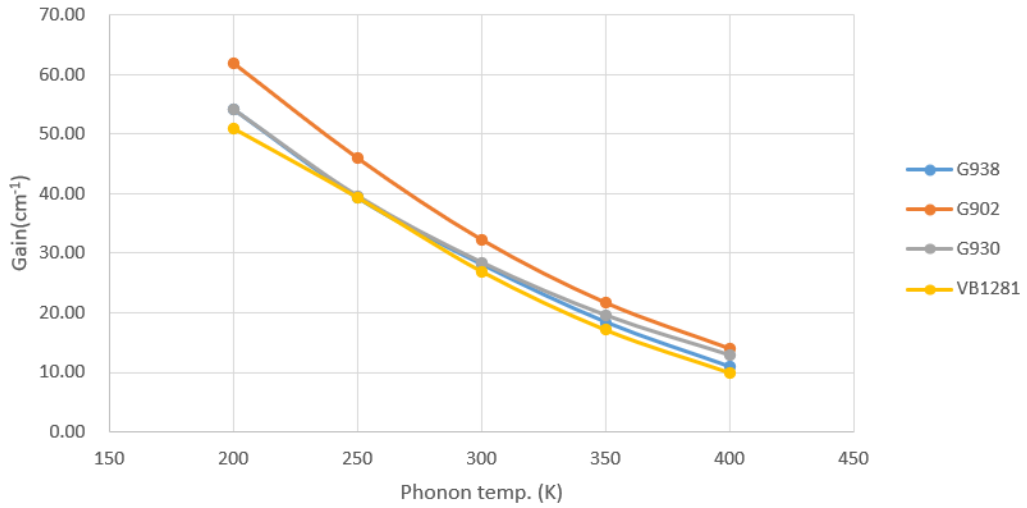

Figure 18: Relationship between phonon temperature and the gain with different structure. The blue line, orange line, grey line and yellow line represents the structure G938, G902, G930 and VB1281 respectively which structures we can get from Ref. [16].

According to Fig.18, we observe that for all structures, as the phonon temperature increases, the corresponding gain gradually decreases. The gain of G902 is relatively higher compared to other structures, with VB1281 exhibiting the lowest gain.

In the study reported in Ref. [16], Ali Khalatpour et al. conducted experiments across various structures, yielding pertinent data for analysis. Interestingly, our simulation outcomes closely mirrored the experimental threshold temperatures (T_{max}) for the G structure, alongside exhibiting similar maximum current density values. However, a notable exception was observed with the VB1281 structure. While experimental data indicated a T_{max} of 232 K and a corresponding highest current density of 2650 A/cm^2, simulation results displayed a T_{max} ranging from 240 K to 250 K, aligning closely with experimental findings. However, the simulated maximum current density was notably lower, measuring only 1600 A/cm^2. To elucidate why the threshold temperature aligns with our T_{max}, we need to consider operational losses encountered during machine operation. Typically, our losses range between 15 and 30 cm^{-1} based on experience, leading us to select a loss value of 20 cm^{-1}. To offset these losses, the gain of the structure must equal or exceed 20 cm^{-1}. If we aim for a higher heatsink temperature, the corresponding gain would decrease, as depicted in Fig.19. Consequently, if our gain just covers our losses, then the heatsink temperature becomes threshold temperature which also can be treated as T_{max} in this scenario. It is worth noting that subtracting normally 90K from the corresponding phonon temperature yields the heatsink temperature.

However, the discrepancy between simulated and experimental values for the VB1281 structure's T_{max} and highest current density prompts further investigation into potential influencing parameters. Notably, the aluminum fraction (x) in the VB1281 structure is smaller than in other structures, impacting the conduction band offset (CBO). In Ref. [15], a CBO equal to x multiplied by 1.01 eV was utilized, consistent with the parameter employed in our previous simulations sourced from the MIT group. However, the ETH group used a CBO equal to x multiplied by 0.831 eV. Consequently, considering the influence of varying CBO values on simulation outcomes might aid in reconciling our results with experimental findings, a topic we explore further in the subsequent chapter.

Overall, in our simulation, the distribution of current density and electron density would influence the gain or we should say the performance of the THz QCL. And the current density distribution and electron density distribution can be influenced by phonon temperature and eFd, thus, this can subsequently affect the value of gain. The gain can be directly affected by population inversion ΔN between ULS and LLS, transition linewidth $\Delta\nu$ and oscillator strength f_{ul}, since peak gain $G_p \propto \Delta N f_{ul}/\Delta\nu$. For our structure, which layer sequence is based on

VB1281, eFd=74mV, phonon temperature is 238K and light frequency is 4.8 THz are the best parameters to generate the highest gain.

Furthermore, we observed a consistent relationship between phonon temperature and gain across different structures, including G938, G902, G930, and VB1281. Specifically, all structures exhibited a trend where gain decreased with increasing temperature. Comparing simulation results with experimental data, we found a close correspondence between the highest threshold temperature, in the simulation and the experimental threshold temperature. Similarly, the highest current density obtained in simulation closely matched the maximum current obtained in experiments for most structures, except for VB1281. In the case of VB1281, the simulated current density was notably lower than the experimental current density, with values of 1600A/cm^2 and 2650A/cm^2, respectively. We speculate that this discrepancy may be attributed to the conduction band offset (CBO), a hypothesis we will investigate further in the upcoming chapter.

5 Modification of conduction band offset

The Conduction Band Offset (CBO) is the height of the barrier due to the different conduction band edge energy between the two different types of layers. It can be expressed by the function of Aluminum fraction x in the barrier. We know that CBO is rather crucial for the THz QCL, since it limits the performance of THz QCL. However, figuring out whether it influences the outcomes of the simulation and how it affects it is more important for us.

From the last chapter, we found that when we set $\mathrm{CBO} = \mathrm{x} \times 1.01\mathrm{eV}$ used in MIT group for VB1281, the current density we tested in the simulation was not that close to the experimental one, but it is very suitable for the G structure. We then hypothesize that if we modify the CBO, it may optimize our current density with VB1281 in our simulation. The reason why we immediately think of CBO is that the aluminum fraction x in the VB1281 structure is smaller than in other structures, and CBO can be expressed by the function of x.

For this reason, in this chapter, we will try the different CBO; that is $\mathrm{CBO} = \mathrm{x} \times 0.831\mathrm{eV}$ used in ETH group rather than $\mathrm{CBO} = \mathrm{x} \times 1.01\mathrm{eV}$ used in MIT group in the structure of VB1281. We will also do the comparation of current density, the highest gain and the frequency of light between these two CBOs in the different structures that are LU2022, LU2022A and LU2022B which structures have been mentioned in Ref. [25]. We will also consider non-linear CBO, which can be expressed by $\mathrm{CBO} = 0.65(1.36 + 0.22x)x$ mentioned in the Ref. [26], using it in the structure of VB1281, LU2022 and G930.

5.1 Different CBO used in VB1281

We used a CBO of x multiplied by 0.831 eV for the VB1281 structure to test whether changing the CBO could yield T_{max} and the highest current values closer to the experimental values in the simulation. Additionally, we aimed to ensure that the corresponding maximum gain could cover the loss set at 20 cm^{-1}. Ultimately, we simulated the VB1281 structure with a CBO of x multiplied by 0.831eV at temperatures of 350K, 300K and 322K, in which 322K corresponds to the T_{max} in experimental result. We found that the highest currents obtained were 2251A/cm^2, 2338A/cm^2 and 2302A/cm^2 respectively. These values are much closer to the experimental value of 2650A/cm^2 compared to the VB1281 structure with a CBO of x multiplied by 1.01eV. This indicates that the choice of CBO does indeed affect the simulation results. A CBO of x multiplied by 1.01eV is more suitable for the G structure, while a CBO of x multiplied by 0.831eV is more suitable for the VB1281 structure.

However, the reason for using different CBO values for the G and VB structures, which is told by Andreas Wacker, Razavipour and Seyed Ghasem to obtain better simulation results lies in the fact that they were grown in different growth places. The G structure was grown by Z. Wasilewski at Waterloo, while the VB structure was grown by J. Reno at Sandia National Labs. Previous studies have indicated that materials grown at the same growth place tend to exhibit similar performance characteristics when tested. Therefore, the choice of CBO tailored to each growth place helps to improve the simulation results for their respective structures. However, different growth place can indeed yield different performance results even for the same structure. This suggests that choice of growth places can influence experimental outcomes. Moreover, even when the same structure is grown at different growth place, the CBO values may vary as well. This variation can be attributed to factors such as differences in experimental conditions, personnel conducting the experiments, and other environmental factors. Therefore, using the same CBO for structures G and VB in simulations may lead to different performance results. Additionally, it's possible that the relationship between CBO and x is nonlinear rather than the linear relationship as we assumed. But this is speculative and requires further investigation for confirmation.

5.2 LU2022& LU2022A& LU2022B

Simulating different CBOs applied to structures other than VB1281 is highly necessary because it allows us to observe whether the results are consistent across different structures, thus demonstrating whether CBO indeed affects the performance of THz QCLs (Table. 4).

Wafer	Seq. (nm)	CBO (eV)	J_{max}^{sim}(kAcm^{-2})	g_{max} (cm^{-1})	f_{sim} (THz)
LU2022(1)	3.1/7.1/2.1/14.2	0.831x	3.26	27.3	3.6
LU2022(2)	3.1/7.1/2.1/14.2	1.01x	2.48	29.6	4.1

Table 4: Two different conduction band offset of the same layer sequence noted as Seq. of LU2022 which are LU2022(1) and LU2022(2). Maximum current densities, maximum gain and the lasing frequencies at a phonon temperature of 300K and x=0.3 are shown.

When we observed that CBO varies, the current density and gain simulated for LU2022 with the same number of layers differ. LU2022(1) with a smaller CBO exhibits a higher current density compared to LU2022(2) with a larger CBO, whereas LU2022(1) shows lower gain compared to LU2022(2). Simultaneously, the frequency of LU2022(1) is also lower than that of LU2022(2). This is because, from quantum mechanics we know that particles can penetrate through a potential barrier even when their energy E is less than the height of the barrier. We refer to this as the tunneling effect, and we can use the transmission coefficient to describe the particle's tunneling ability. The transmission coefficient can be described as

$$D = D_0 e^{-\frac{2}{\hbar}\sqrt{2m(U_0-E)}a} \quad (18)$$

Where U_0 is the value of the highest potential energy point of the square potential barrier, E is the energy of the particle, and a is the width of the barrier. We can see that the transmission coefficient sharply decreases with the widening or heightening of the barrier, while a decrease in CBO indicates a reduction in the height of the barrier. Consequently, an increase in the transmission coefficient allows electrons to more easily pass through the barrier, resulting in a greater current, while fewer photons are generated, leading to a decrease in gain. This explains why LU2022(1) with a smaller CBO has a higher current density and lower gain compared to LU2022(2). Moreover, the decrease in CBO results in a smaller energy difference, consequently leading to a decrease in the obtained frequency.

To further validate this interpretation, we also simulated LU2022A and LU2022B of which structures have been mentioned in Ref. [25]. We simulated different CBOs for each structure and obtained the following results (Table. 5).

Wafer	Seq. (nm)	CBO (eV)	J_{max}^{sim} (kAcm^{-2})	g_{max} (cm^{-1})	f_{sim} (THz)
LU2022A (1)	3.1/7.3/2.2/14.2	0.831x	3.21	24.8	2.9
LU2022A (2)	3.1/7.3/2.2/14.2	1.01x	2.47	25.3	3.2
LU2022B (1)	3.1/7.6/2.4/14.2	0.831x	3.15	17.7	1.9
LU2022B (2)	3.1/7.6/2.4/14.2	1.01x	2.48	20.6	1.9

Table 5: Two different conduction band offset of LU2022A with the same layer sequence which are LU2022A (1) and LU2022A (2). And Two different conduction band offset of LU2022B with the same layer sequence which are LU2022B (1) and LU2022B (2). Maximum current densities, maximum gain and the lasing frequencies at a phonon temperature of 300K and x=0.3 are shown.

Eventually, we found that even for LU2022 structures with different layer sequences, the results exhibit consistency. Specifically, when the layer sequences were the same, structures with smaller CBOs exhibited higher current and lower gain.

5.3 Non-linear Conduction Band Offset

Through previous simulations, we found that the value of CBO can indeed affect the simulation results, such as the highest current density and the gain. As an aside aspect, it is useful to present here an argument of why we can change the value of CBO. As in normal circumstances, the value of CBO should be determined along with the layer sequence. This is because, in real experiments, CBO is unmeasurable, or rather, difficult to measure. Therefore, we need to predict its magnitude in simulations to see which value results in simulation results closer to experimental results. Additionally, the value of CBO is definitely related to x which is the fraction of Aluminum in GaAs/$Al_xGa_{1-x}As$, so guessing the size of CBO is essentially a linear or nonlinear relationship with x.

However, the CBOs we previously set were linear, and this prompted us to explore the impact of introducing nonlinearity into our simulations. We were intrigued by how altering the CBO to a nonlinear form would affect the results. Therefore, we decided to employ LU2022 with a CBO of $0.65(1.36 + 0.22x)x$, a parameter also referenced in Ref. [26]. The rationale behind choosing this nonlinear function as the CBO lies in its consistency with the experimental observations and calculations of Razavipour and Seyed Ghasem. Particularly, it aligns well with their findings regarding electric field alignment and Negative Differential Resistance (NDR). As such, we anticipated that this adjustment would provide valuable insights into the behavior of our system. Subsequently, the results we obtained are detailed below. And we do the comparation between the different CBOs in the structure of VB1281, LU2022 and G930 (Table. 6).

For a CBO that exhibits a nonlinear relationship with x, its impact on maximum current densities J_{max}^{sim} and lasing frequencies and the maximum gain is consistent with that of a linear CBO. Specifically, as the CBO increases, J_{max}^{sim} decreases while the maximum gain g_{max} increases. If we aim for larger J_{max}^{sim} that are closer to experimental values and smaller f_{sim}, we can achieve this by using a smaller CBO. However, extensive experimentation and simulations are still required. These endeavors allow us to observe the impact of nonlinearity on simulation results. Specifically, we need to assess whether under the same temperature and x conditions, the J_{max}^{sim}, g_{max} and f_{sim} obtained through simulations for different layer sequences with a nonlinear CBO align with experimental findings. Due to the limited availability of experimental data, this particular research segment holds significant potential in laying the foundation for future investigations into nonlinear CBO. By delving into the effects of nonlinear CBO on simulation results and comparing them with available experimental data, we can uncover valuable insights into the behavior of THz QCL under varying conditions.

Wafer	Seq. (nm)	CBO (eV)	x	J_{max}^{sim} (kAcm^{-2})	g_{max} (cm^{-1})	f_{sim} (THz)
VB1281 (1)	3.84/6.97/2.42/14.5	0.831x	0.25	2.34	26.1	3.6
VB1281 (2)	3.84/6.97/2.42/14.5	1.01x	0.25	1.63	26.9	4.4
VB1281 (3)	3.84/6.97/2.42/14.5	$0.65(1.36+0.22x)x$	0.25	2.10	26.5	3.9
LU2022 (1)	3.1/7.3/2.2/14.2	0.831x	0.3	3.3	27.3	3.6
LU2022 (2)	3.1/7.3/2.2/14.2	1.01x	0.3	2.5	28.6	4.1
LU2022 (3)	3.1/7.3/2.2/14.2	$0.65(1.36+0.22x)x$	0.3	2.91	27.7	3.9
G930(1)	3.04/7.25/1.91/14.6	0.831x	0.35	2.29	28	4.1
G930(2)	3.04/7.25/1.91/14.6	1.01x	0.35	2.05	28.4	4.6
G930(3)	3.04/7.25/1.91/14.6	$0.65(1.36+0.22x)x$	0.35	2.37	30.5	4.4

Table 6: Three different structures VB1281, LU2022 and G930, with the different CBO of $0.831x$, $1.01x$ and $0.65(1.36+0.22x)x$, which are denoted as (1) (2) and (3). Maximum current densities, maximum gain and the lasing frequencies at a phonon temperature of 300K are shown.

Thus, we had some suggestions on which CBO is suitable for different structures, for example, CBO=0.831x is suitable for VB1281, but CBO= $0.65(1.36+0.22x)x$ is suitable for G930 since we got the highest current density in our simulation by using those CBOs with different structures are similar with experimental results. However, we can't tell which CBO is the best one for different structures, since we had a lot of choices of CBO, and we can't choose which specific function of CBO is the most suitable function for all the structures. This is because different samples grew in different growth places, they treated different CBO. But what we can further study is that we can scan the value of CBO or x to find which value is best for the structures.

In conclusion, we utilized a different CBO value in VB1281, where it equals 0.831x instead of the originally simulated CBO of 1.01x. We observed that in simulations at T_{max}=322K, the J_{max}^{sim} obtained using CBO=0.831x is closer to the experimental values. This indicates that in VB1281, it is more appropriate to use CBO=0.831x. Furthermore, we also observed that as CBO decreases, J_{max}^{sim} increases, while g_{max} and f_{sim} decrease. This provides us with a promising approach to achieving frequencies lower than 4 THz for THz light generation. However, the drawback is that the maximum gain obtained may decrease. This phenomenon arises because as CBO decreases, the corresponding barrier height

decreases, leading to an increase in the transmission coefficient. As a result, electrons are more likely to tunnel through the barrier, resulting in a higher current. However, this also leads to a reduction in the number of photons generated, hence decreasing the gain. Additionally, the decrease in barrier height also results in a reduction in the energy difference, leading to a cut down in the frequency of the generated THz light.

We also found that the results obtained from VB1281, LU2022, G930 in the simulation, as well as VB1281, are consistent which is that as the CBO decreased, J_{max}^{sim} increased while g_{max} and f_{sim} reduce. And we applied $CBO = 0.65(1.36 + 0.22x)x$ which is non-linear to structures VB1281, LU2022 and G930, finding that it yielded consistent results with the linear relationship between CBO and x. Nevertheless, to verify whether the results obtained from simulating with nonlinear CBO are consistent with experimental results, we would require a substantial amount of experimental data for validation. For this reason, this part of investigation establishes a basis for accurately forecasting CBO in the future.

6 Modification of the doping density

In order to have electrons in the conduction band of the structure the samples are n-doped. Here the doping with a given volume density n_{3D}, is located in a certain range within each module. For the samples considered here, this is a range of 3 nm in the middle of the wide well. The product between volume density and range provides the areal doping density n_{2D}, which equals the areal doping density of electrons in each module for charge neutrality.

When modifying the CBO of LU2022(2), we encountered an error in the doping density parameter we set, since we mistakenly took the sheet doping density per module which is $n_{2D} = 4.5 \times 10^{10}\mathrm{cm}^{-2}$ mentioned in Ref. [15] as the required volume doping density which is $n_{3D} = 1.5 \times 10^{17}\mathrm{cm}^{-3}$. Only by $\frac{n_{2D}}{w}$, where w is the total length of doping positions (Fig. 8), can we obtain the volume doping density. Accordingly, the resulting highest current and the maximum gain are particularly small, especially are $1.1 \times 10^{-6}\mathrm{kAcm}^{-2}$ and $1.5 \times 10^{-5}\mathrm{cm}^{-1}$, at 300K. Consequently, we can consider whether the volume doping density can achieve higher highest current and larger gain. Thus, in this chapter, we investigate the relationship between volume doping density and both the gain and the highest current to modify doping density in LU2022(2) at 300K.

6.1 Relationship between n_{2D} and the highest current density

We conducted simulations of the highest current density at 300K for various volume doping densities in LU2022(2). Fig. 19 illustrates the relationship between volume doping density and the highest current density. We observed that as the volume doping density increases, the highest current density increases. This phenomenon elucidates why a smaller volume doping density setting corresponds to a lower highest current density. The underlying reason for this correlation is that

$$\mathrm{J} = \frac{n_{2D}}{\tau_{transit}} e, \tag{19}$$

where J is the highest static current, $\tau_{transit}$ is the typical time of electrons transport to the next module which normally is 1ps and e is the value of charge of an electron. Hence, from this relationship, we can infer that there exists a linear correlation between the volume doping density and the highest current. As the volume doping density increases, the higher current density we get. Although we could observe in our simulation in Fig. 19 that the highest current density does increase with rises in doping density, the relationship is non-linear. The rapid initial increase in current density followed by a slower growth is attributed to the imperfections in the material caused by the increasing doping density, leading to more electron scattering and ultimately resulting in a decelerate increases in the

highest current density with the rises in doping density. While a higher maximum current is desirable, it should not be excessively high, as this could lead to overheating, potentially damaging the device.

It is worth noting that when the doping density is remarkably high, such as at a density of $1.5 \times 10^{18}\ \mathrm{cm}^{-3}$, achieving the highest current density requires a larger bias drop (eFd) compared to lower doping densities. This is because when the doping density is too high, more electrons are generated, leading to ionization and the attraction of more positive ions. This region is delineated in Fig. 20 by a black square. Additionally, a large number of electrons will tunnel from the ground state to the next module's ULS, resulting in an accumulation of electrons in the area marked by the blue square in Fig. 20. The increase in positive ions in the doping area causes a decrease in the potential of this region. Conversely, in the region marked by the blue square, the rise in electrons leads to an increase in potential. Both the increase and decrease in potential can be observed in Fig. 20. Consequently, due to these fluctuations in potential, the ground state in the doping area decreases, while the ULS in the blue square area increases. This prevents the electrons from remaining in the ground state and facilitates their tunneling to the ULS in the next module. Therefore, a larger bias drop is required to elevate the ground state and facilitate electron tunneling to the ULS. This is why a larger bias drop is necessary at higher doping densities.

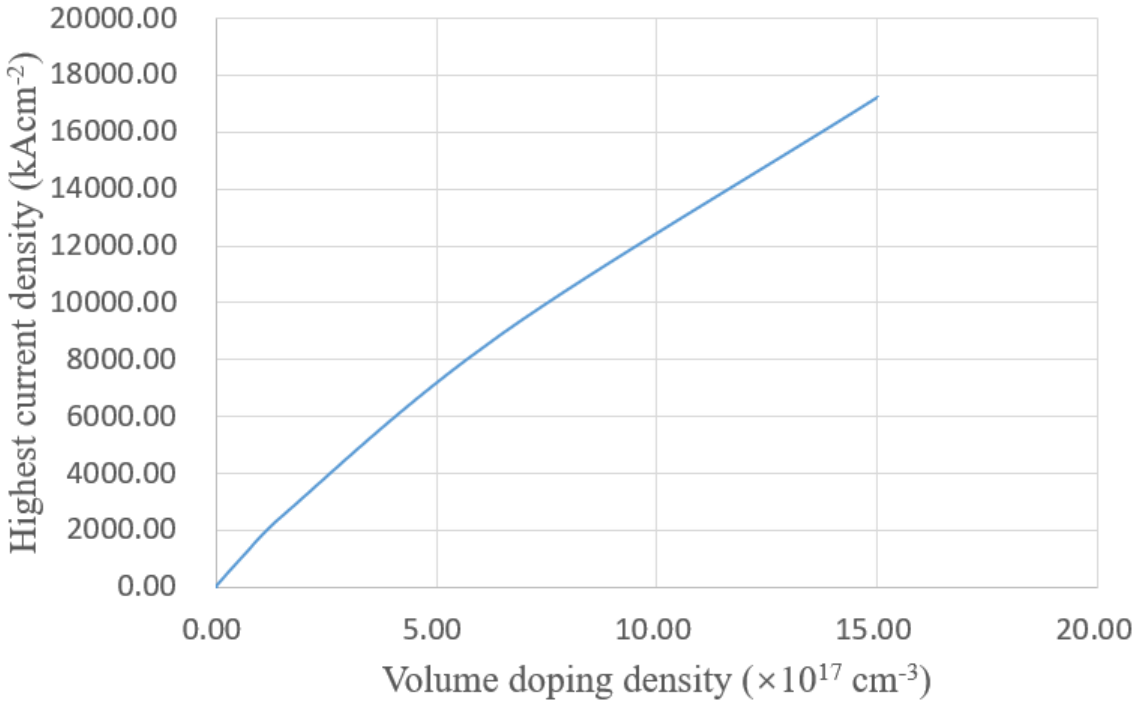

Figure 19: Relationship between volume doping density and the highest current density.

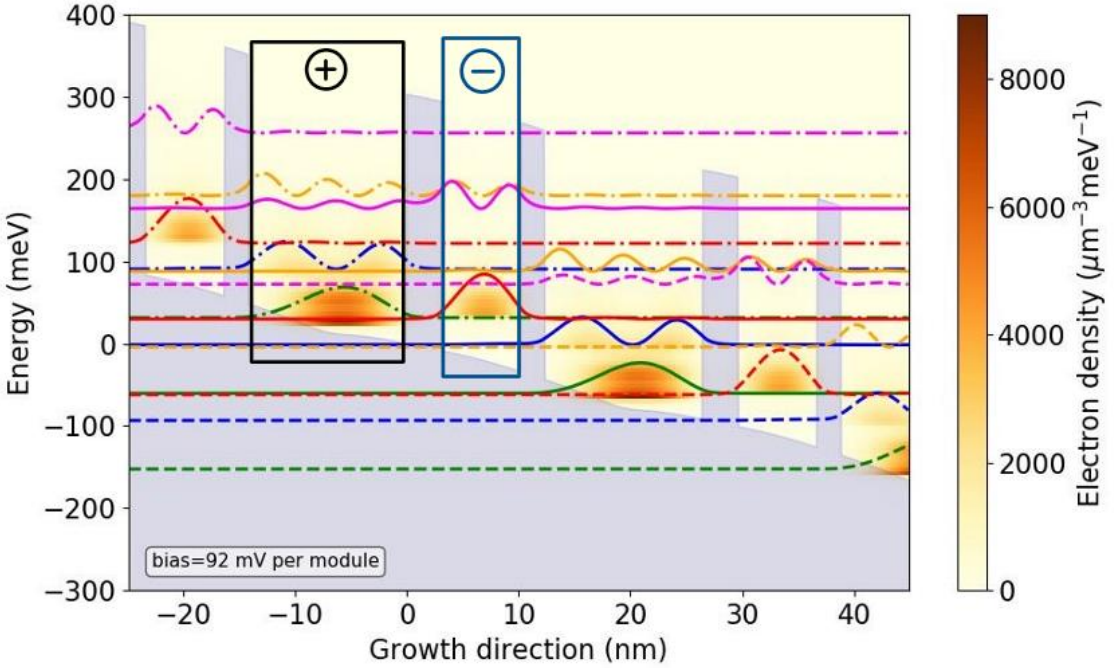

Figure 20: Electrons density distribution with volume doping density 1.5×10^{18} cm^{-3} and bias drop is 92mV at 300K.

6.2 Relationship between n_{2D} and the gain

We determined the relationship between the volume doping density and the gain shown in figure 21. We observed that the highest current will rise with the elevation of volume doping density n_{3D}, however, after reaching its peak, the gain will decrease with the increase in doping density. This is because the high doping density leads to more defects, resulting in a shorter lifetime of energy levels. A shorter lifetime leads to an increase in transition linewidth, as discussed in chapter 4 with the relevant equation which is $\Delta\nu = \frac{1}{2\pi}\left(\frac{1}{\tau^u} + \frac{1}{\tau^l} + \frac{2}{T^*}\right)$. And we know that the rate of stimulated emission and absorption between ULS and LLS is given by [23]

$$R^{opt}_{ULS\rightarrow LLS} = \frac{1}{\hbar}\left|\frac{F_{ac} d_{ULS,LLS}}{2}\right|^2 (n_{ULS} - n_{LLS}) \frac{\gamma}{(E_{ULS} - E_{LLS} - \hbar\omega)^2 + \frac{\gamma^2}{4}} \quad (20)$$

where F_{ac} is time independence part of oscillating field, $d_{ULS,LLS}$ is distance between ULS and LLS, n_{ULS} and n_{LLS} are number of electrons on ULS and LLS. E_{ULS} and E_{LLS} are energy of ULS and LLS. γ is width of the transition, $\Delta\nu$ can be got by $\gamma/\hbar$. This rate can be directly translated to the gain. [23]

So, from this equation we can see that as γ rises, which means that lifetime decreases, $R^{opt}_{ULS\to LLS}$ goes down, the gain decreases as well, only when we consider it is peak gain then we can neglect $(E_{ULS} - E_{LLS} - \hbar\omega)^2$.This is why when the doping density takes excessively high values, gain decreases as it increases. In our simulations, we can verify this. From Fig. 22, we observed that γ at $1.5 \times 10^{18}\text{cm}^{-3}$ is wider than γ at $6.5 \times 10^{17}\text{cm}^{-3}$, but the gain at $1.5 \times 10^{18}\text{cm}^{-3}$ is smaller than the gain at $6.5 \times 10^{17}\text{cm}^{-3}$,which is consist with our deduction.

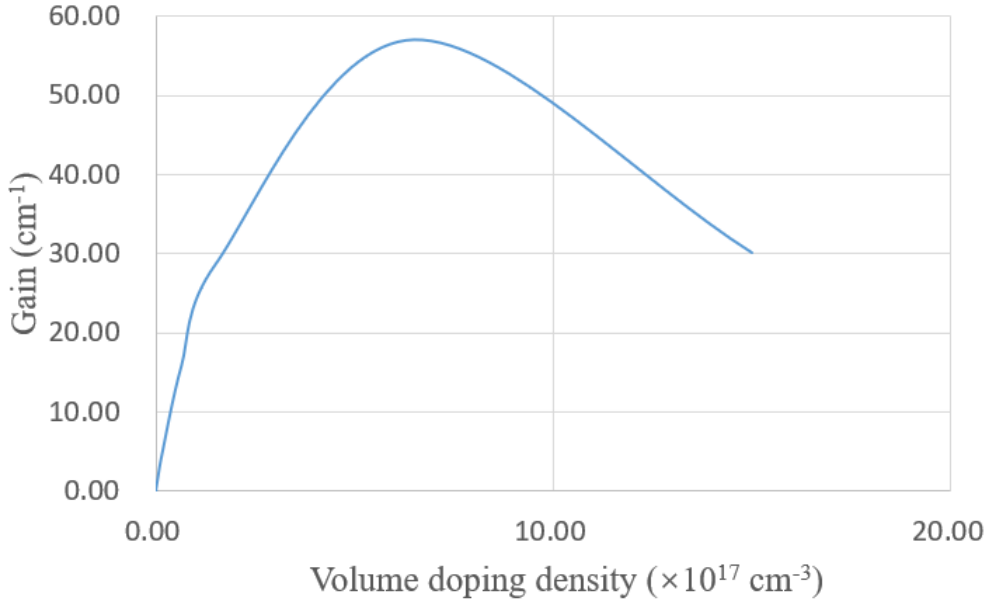

Figure 21: Relationship between volume doping density and the gain.

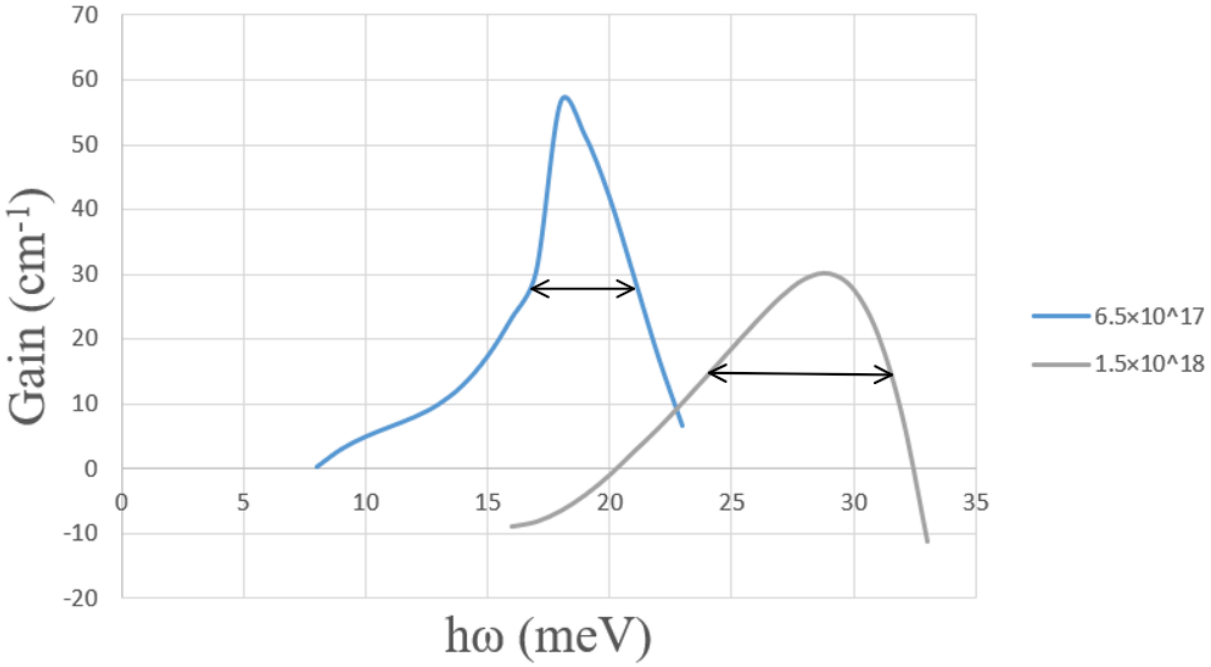

Figure 22: Relationship between $h\omega$ and the gain at doping density are $6.5 \times 10^{17}\text{cm}^{-3}$ (blue curve) and $1.5 \times 10^{18}\text{cm}^{-3}$ (grey curve) respectively. FWHM is marked in the figure.

To summarize, in this chapter, we have explored the relationship between the volume doping density and both highest current and gain, where highest current density increases with the rise in n_{3D}, but it is nonlinear which is not consistent with theoretical derivation due to impurity in the semiconductor. Conversely, the gain exhibits an increase at the initial growth stage of n_{3D}, followed by a decrease as n_{3D} continues to grow due to shorter lifetime. Therefore, if we aim for higher highest current density or greater gain, increasing n_{3D} might be one of the potential solutions, but it can't be too high because if highest current density is too high then result in high temperature which would damage the machine and gain would also decrease.

7 Conclusions

In this thesis, our efforts to identify the factors limiting the performance of THz QCLs have led to several key findings. Initially, we focused on modifying the energy difference to enhance the generation of terahertz light. Through simulations, we determined that for structures with 3 energy levels and 2 quantum wells, achieving a higher current density is possible when the Aluminum fraction (x) is around 0.3. This facilitates efficient electron tunneling from the ground state to the upper lasing state (ULS), thus boosting terahertz light production. Additionally, optimizing the bias drop (eFd) around 0.074meV helps attain the highest current density and mitigates thermal backfilling effects, enhancing THz QCL performance. Similar trends were observed for structures with 5 energy levels, indicating the utility of simplified 3-level models for valuable simulation insights.

Subsequently, we delved into the relationship between electron density distribution, current density distribution, and gain, recognizing gain as a pivotal parameter for describing THz QCL performance. Our exploration revealed that eFd and temperature (T) exert significant influence on current density and, consequently, on gain. Moreover, temperature can affect electron density distribution, further modulating gain. This underscores the importance of temperature, along with current density and electron density distribution, in shaping THz QCL performance. Additionally, we elucidated that peak gain is directly impacted by transition linewidth and oscillator strength, thereby affecting overall device performance.

Furthermore, our investigation into the conduction band offset (CBO) highlighted its role in influencing key performance metrics such as maximum current density (J_{max}^{sim}), maximum gain (g_{max}), and light frequency (f_{sim}). Notably, smaller CBO values were associated with increased J_{max}^{sim}, albeit at the expense of reduced g_{max} and f_{sim}, thereby impacting THz QCL performance.

Moreover, we explored the impact of volume doping density on gain and highest current density, revealing a positive correlation between doping density and these performance metrics. However, further increases in doping density led to a decline in gain, underscoring the nuanced influence of doping on THz QCL performance.

Overall, these findings shed light on the intricate interplay between various parameters and their effects on THz QCL performance, providing valuable insights for optimizing device design and operation.

We found that the frequency of terahertz light obtained in certain structures is less than 4THz and the gain is greater than 20cm^{-1}, which can cover the losses close to the room temperature. The results can be found in table 6.

Besides, we have discovered that to decrease the frequency of terahertz light, one can achieve this by reducing the CBO. Nevertheless, the drawback of this approach is that it leads to a lower gain.

8 Outlook

The primary objective of this work is to pinpoint the factors constraining the performance of THz QCLs. Our subsequent goal is to ascertain the optimal structure, which entails identifying the parameters in simulations that yield the highest-performing THz QCL. Concurrently, it's imperative to continue uncovering additional factors limiting the performance of THz QCLs. Regarding the nonlinearity of CBO, we've solely simulated the impact of CBO on simulation results. However, there's a paucity of experimental data to verify whether nonlinear CBO can outperform linear CBO, thereby bringing simulation results closer to experimental findings. Thus, it's crucial to compare experimental data with simulation results using nonlinear CBO. Ideally, finding the optimal CBO such that simulation outcomes consistently align with experimental results across different structures would be advantageous.

Additionally, in my research, we just scanned one parameter at the time, such as bias drop (eFd) in Fig. 12, temperature in Fig. 13 and volume doping density in Fig. 19 to see how a single parameter influence the simulation results and find the optimal parameter. We have known that impact experimental results not only by one parameter, so it is necessary that scan more than one parameter. For example, scan temperature and volume doping density at the same time and to find the optimal temperature and volume doping density as well, resulting in the 3D diagram with the relationship between temperature, volume doping density and gain. However, it is time consuming when we scan two or more parameters together. In my simulation, even if we scan only one parameter, we still need almost half of day to get our results. Thus, we will not continue to simulate this in our study. This can serve as direction for further research, as the parameters still have a significant impact on the experiment. Therefore, this research in this field has considerable potential for development.

Furthermore, due to variations in parameters, the results of simulations and experiments can differ. We know that differences in settings such as CBO, volume doping density and etc. can lead to discrepancies between simulation and experimental results. Additionally, inaccuracies in the active region structure and calculation model predictions can also cause differences between the simulation and experimental results. However, differences in the interface roughness parameter, which provides scattering due to imperfections of the interfaces between two semiconductor layers, can cause discrepancies between the simulation and experimental results as well, as discussed in Ref. [31]. In fact, the reasons for the differences between experimental and simulation results could be due to a combination of multiple factors or the cumulative effect of several parameters. Therefore, to achieve simulation results that more closely match the

experiment results, further exploration and investigation are needed. This is also what made this project fascinating.

Finally, given the substantial demand for terahertz light in diverse applications such as security screening and biomedical applications, the efficient generation of terahertz light using THz QCLs holds particular significance. In conclusion, research on THz QCLs remains highly promising, and we hope that this thesis can contribute to the advancement of THz QCLs.

References

[1] Xu Meng et al. *Multi-band terahertz 4 × 2 encoder based on two-dimensional photonic crystal.* Optical Communication Technology. 2023, O734; O441.4.

[2] Jiahao Huang et al. *Photonic and electric control in terahertz quantum cascade lasers: Review. Journal of Infrared Millim.* Waves, 2022, 41(01), 169-180. DOI : 10.11972/j.issn.1001-9014.2022.01.012

[3] Zhanglong Fu et al. *Progress in biomedical imaging based on terahertz quantum cascade lasers.* Chinese Journal of Laser, 2020, 47(02), 185-194

[4] Zhiyong Tan et al. *Progress in real-time imaging based on terahertz quantum-cascade lasers.* Chinese Optics, 2017, 10(01), 68-76

[5] Xiaoyong He, *Investigation Electron Transport in Therahertz Quantum Cascade Laser and Waveguide.* Doctoral thesis. University of Chinese Academy of Sciences, 2007.

[6] Boyu Wen and Dayan Ban, *High-temperature terahertz quantum cascade laser.* Progress in Quantum Electronics, 2021, 80, 100363. DOI: 10.1016/j.pquantelec.2021.100363.

[7] R. Köhler et al. *Terahertz semiconductor herterostructure laser.* Nature, 2002, 417(6885): 156-159.

[8] Yongquan Zeng et al. *Photonic Engineering Technology for the Development of Terahertz Quantum Cascade Lasers.* Adv. Optical Mater, 2020,8(03),1900573. DOI: 10.1002/adom.201900573

[9] L. H. Li et al. *High-power GaAs/AlGaAs quantum cascade lasers with emission in the frequency range 4.7-5.6 THz*// International Quantum Cascade Lasers School and Workshop. 2016. https://www.researchgate.net/publication/308361990_Highpower_GaAsAlGaAs_quantum_cascade_lasers_with_emission_in_the_frequency_range_47-56_THz

[10] Ali Khalatpour et al. *High-power portable terahertz laser sysytems.* Nature Photonics, 2021, 15: 16-20. DOI: 10.1038/s41566-020-00707-5

[11] Wenjian Wan et al. *Research Progress on Terahertz Quantum Cascade Laser.* Chinese Journal of Lasers, 2020, 47(07), 106-118

[12] Zhaolong Xu, *Research on self-mixing interference technology of terahertz quantum cascade laser.* Master thesis. Shandong University, 2020.

[13] Andreas Wacker, Gunnar O and Stephanie R. Quantum Mechanics. Lund University, 2013.

[14] Shixun Zhou, course on quantum mechanics. Higher Education Press, Beijing, 2009.

[15] Viktor Rindert et al. *Analysis of High-Performing Terahertz Quantum Cascade Lasers.* Phys. Rev. Applied, 2022, 18(04), L041001. DOI: 10.1103/PhysRevApplied 18.L041001

[16] Ali Khalatpour et al. *Enhanced operating temperature in terahertz quantum*

cascade lasers based on direct phonon depopulation. Appl. Phys. Lett. 2023, 122(16),161101. DOI: 10.1063/5.0144705
[17] Viktor Rindert, *Simulation of THz Quantum Cascade Lasers.* Master thesis. Lund University, 2021.
[18] Ali Khalatpour et al. *High-power portable terahertz laser systems.* Nature Photonics 15, 16-20. DOI: 10.1038/s41566-010-00707-5 (2021)
[19] Andreas Wacker, *Quantum Cascade Laser: An Emerging Technology in Nolinear Laser Dynamics (ed Lüdge, K.)* (Wiley-VCH, Berlin, 2012)
[20] Jonathan A. Fan et al. *Surface emitting terahertz quantum cascade laser with a double-metal waveguide.* Opt Express. 2006, 14(24): 11672-11680. DOI: 10.1364/oe.14.011672.
[21] Chenren Yu, *Mode Selection and Tailoration of the Radiation Efficiency in Terahertz Quantum Cascade Lasers.* Doctoral thesis. University of Chinese Academy of Sciences, 2020.
[22] Andreas Wacker, personal communication. Dec. 11, 2023.
[23] Andreas Wacker, *Mid-Infrard and Terahertz Quantum Cascade Lasers.* B. Dan and B. Mikhael. Cambridge University Press, Cambridege, 2023. Simulating Quantum Cascade Lasers: The challenge to quantum theory: 153-172.
[24] David Winge, *Quantitative Modeling of Gain in Quantum Cascade Lasers under Operational Intensities.* Doctoral thesis. Lund University, 2016.
[25] Denizhan Ekin Önder, *Dynamical Analysis of Terahertz Quantumm Cascade Lasers.* Doctoral thesis. Lund University, 2023.
[26] Seyed Ghasem Razavipour, *Design, Analysis, and Characterization of Indirectly-pumped Terahertz Quantum Cascade Lasers.* Doctoral thesis. University of Waterloo, 2013.
[27] Hailong Wang et al. *Electron-electron Scattering Rate in Ga InAsP/Inp Stepped Quantum Well.* Chinese Journal of Luminescence, 2016, 37(11): 1408-1414.
[28] Juan Song, *First-principles study on the structure and physical properties of $Al_xGa_{1-x}As$ Materials.* Journal of synthetic crystals, 2020, 49(05), 824-832. DOI: 1000-985X(2020)05-0824-09
[29] Chuandao Wang, *Electronic structure in GaAs/ $Al_xGa_{1-x}As$ spherical quantum dots.* Acta Phys. Sin., 2008, 57(2): 1091-1096. DOI: 10.7498/aps.57.1091.
[30] Andreas Wacker et al. *Nonequilibrium Green's Function Model for Simulation of Quantum Cascade Laser Devices Under Operating Conditions.* IEEE Journal of Selected Topics in Quantum Electronics, 2013, 19(05), 1-11.
[31] K. A. Krivas et al. *Influence of interface roughness in quantum cascade lasers. Journal of applied physics.* 118, 114501(2015). DOI: 10. 1063/1.493072.